Journal of Physics D: Applied Physics



# Transformer Coupled Toroidal Wave-Heated Remote Plasma Sources Operating in in Ar/$NF_3$ Mixtures

To cite this article before publication: Scott James Doyle *et al* 2024 *J. Phys. D: Appl. Phys.* in press https://doi.org/10.1088/1361-6463/ad660f

# Transformer Coupled Toroidal Wave-Heated Remote Plasma Sources Operating in Ar/$NF_3$ Mixtures

Scott J. Doyle[1], Amanda Larson[2], Guy Rosenzweig[2], James Gunn[2], and Mark J. Kushner[1,3]

[1] University of Michigan, Dept. of Electrical and Computer Engineering, 1301 Beal Ave., Ann Arbor, MI 48109-2122, USA
[2] MKS Instruments, 90 Industrial Way, Wilmington, MA 01887, USA
[3] Author to whom correspondence should be addressed
e-mails: scott.doyle@physics.org, amanda.larson@mksinst.com, guy.rosenzweig@mksinst.com, jim.gunn@mksinst.com, mjkush@umich.edu

## Abstract

Remote plasmas are used in semiconductor device manufacturing as sources of radicals for chamber cleaning and isotropic etching. In these applications, large fluxes of neutral radicals (e.g., F, O, Cl, H) are desired with there being negligible fluxes of potentially damaging ions and photons. One remote plasma source (RPS) design employs toroidal, transformer coupling using ferrite cores to dissociate high flows of moderately high pressure (up to several Torr) electronegative gases. In this paper, results are discussed from a computational investigation of moderate pressure, toroidal transformer coupled RPS sustained in Ar and Ar/$NF_3$ mixtures. Operation of the RPS in 1 Torr (133 Pa) of argon with a power of 1.0 kW at 0.5 MHz and a single core produces a continuous toroidal plasma loop with current continuity being maintained dominantly by conduction current. Operation with dual cores introduces azimuthal asymmetries with local maxima in plasma density. Current continuity is maintained by a mix of conduction and displacement current. Operation in $NF_3$ for the same conditions produces essentially complete $NF_3$ dissociation. Electron depletion as a result of dissociative attachment of $NF_3$ and $NF_x$ fragments significantly alters the discharge topology, confining the electron density to the downstream portion of the source where the $NF_x$ density has been lowered by this dissociation.

## I. Introduction

Remote plasma sources facilitate the production of neutral radicals for use in materials processing reactors while minimizing exposure of materials to significant fluxes of charged species and photons [1,2]. A remote plasma source (RPS) typically employs either or both of biased grids or long flow distances from the plasma source to the reactor to isolate charged particles or to allow for recombination of charged particles. These designs result in radical fluxes to the substrate having a low charged particle fraction. RPSs are employed for chamber cleaning [3-5], photoresist stripping [6-8], isotropic chemical etching [9-12], atomic layer etching [13,14], atomic layer deposition [15,16], and chemical vapor deposition [17,18]. RPSs are increasingly being investigated for use in selective isotropic etching processes, and particularly for the manufacture of horizontally stacked nano wires and gate-all-around architectures [11,19].

RPSs are often employed when high radical fluxes are required [1], necessitating high plasma densities ($> 10^{12}$ cm$^{-3}$) and high flow rates (up to many slm) of feedstock gases. As such, internal components of the RPS can be exposed to harsh conditions, including high radical and radiative fluxes to plasma-facing surfaces and high gas temperatures (>2000 K) [20] resulting in erosion through reactions with these chemically reactive species [4]. Design challenges for RPSs are demanding, which motivate the use of chemically inert internal surfaces and electrodeless power coupling schemes capable of operating at high temperatures.

High plasma density RPSs use a variety of power schemes, including radio frequency (RF) capacitively coupled plasma (CCP) [9,15], RF inductively coupled plasma (ICP) [11], microwave coupled [5], and transformer coupled [2,21]. Toroidal transformer coupled plasma (TTCP) sources are an attractive option. In conventional ICP sources, the electromagnetic wave delivering power to the plasma is directly launched into the chamber from the antenna through a dielectric window. Similar to a tokamak, TTCP sources employ an external primary coil antenna driven by an RF current which is wrapped around and induces a magnetic field inside a ferrite loop. The ferrite guides and focuses the magnetic field, which is delivered to the plasma chamber where a toroidal electric field is induced, producing the plasma. Prior studies have addressed transformer coupled RPSs in continuous-wave (CW) operation employing electronegative gas admixtures including $NH_3$ [2,22], $NF_3$ [4,23,24,25], $CF_4$ [26], $O_2$ [24] and $SF_6$ [27]. A typical system layout of the RPS and, for example, a plasma etching chamber receiving its output will strategically optimize the length of the flow tube between the RPS and the chamber [25]. The tube length should be short to

deliver the plasma produced radical with a minimum of recombination. The tube should be long to minimize the likelihood for plasma reaching the chamber. While the applications of RPSs have been highlighted in low-temperature plasma roadmaps [28], there have been few fundamental studies of RPS plasma properties and transformer-coupled source design.

Commercial use of transformer coupled RPSs is well established [18,29-31]. However, since the integration of plasma diagnostics is difficult in high plasma density sources having these operating conditions, diagnostics are often limited to downstream measurements of radical densities or reaction products. Design of RPSs using the TTCP configuration would benefit from an improved understanding of their fundamental operation.

In this paper, we discuss results from a computational investigation of a toroidal, transformer coupled RPS sustained Ar and Ar/$NF_3$ mixtures for conditions typically used for semiconductor manufacturing (1 Torr, 1 kW). TTCP operation using a single ferrite core in argon produced a continuous plasma loop with a maximum plasma density of $1.1 \times 10^{13}$ $cm^{-3}$, and with power deposition and ionization occurring nearly uniformly along the azimuthal current loop. Transformer current in the azimuthal direction is largely sustained by conduction current. When operating with dual-ferrite cores, azimuthal asymmetries are introduced resulting in local maxima in power deposition and plasma density. The introduction of $NF_3$ significantly depletes the upstream electron density by dissociative electron attachment, breaking the continuous plasma loop, and resulting in a low-density ($10^{10}$ - $10^{11}$ $cm^{-3}$) $F^-/NF_x^+$ ion-ion plasma upstream of the ferrites. Transformer current is maintained by both conduction and displacement current.

The numerical model, simulation geometry, and operating conditions are discussed in Sec. II. Operation of a TTCP in argon using single and dual ferrite core configurations is discussed in Sec. III. Plasma properties of TTCPs operating in Ar/$NF_3$ mixtures are discussed in Sec. IV and concluding remarks are in Sec. V.

## II. Description of the Model and Conditions

Two configurations of the TTCP-RPS were investigated having single and dual-ferrite cores. This 2-dimensional (2D) geometry was motivated by commercial designs of RPS. For an example of a similar transformer-coupled Ar/$NF_3$ attached to a plasma etching chamber see Yeom et. al. [25]. The computational domain is 22.8 cm by 20.8 cm using a rectilinear, numerical mesh of 91 cells wide × 83 cell high using Cartesian coordinates, yielding a resolution of 0.25 cm/cell.

A uniform depth of 3.25 cm is specified to enable computation of volumetric properties such as gas residence time and power density based on absolute values of flow rates, power and current, but otherwise does not affect the calculation. Feed gas enters through a 3.0 cm long inlet tube into the 3.25 cm wide toroidal vessel tube. Gas exits the source through a 5.0 cm long outlet tube. The walls of the inlet and outlet tubes are grounded while all other plasma facing surfaces consist of 0.5 cm thick alumina. The inlet gas flow rate was 500 sccm of either pure argon or Ar/$NF_3$ mixtures. A pressure of 1 Torr is specified as a boundary condition at the outlet maintaining a pressure of approximately 1 Torr (± 0.1 Torr) throughout the source. The walls of the chamber were maintained at 325 K.

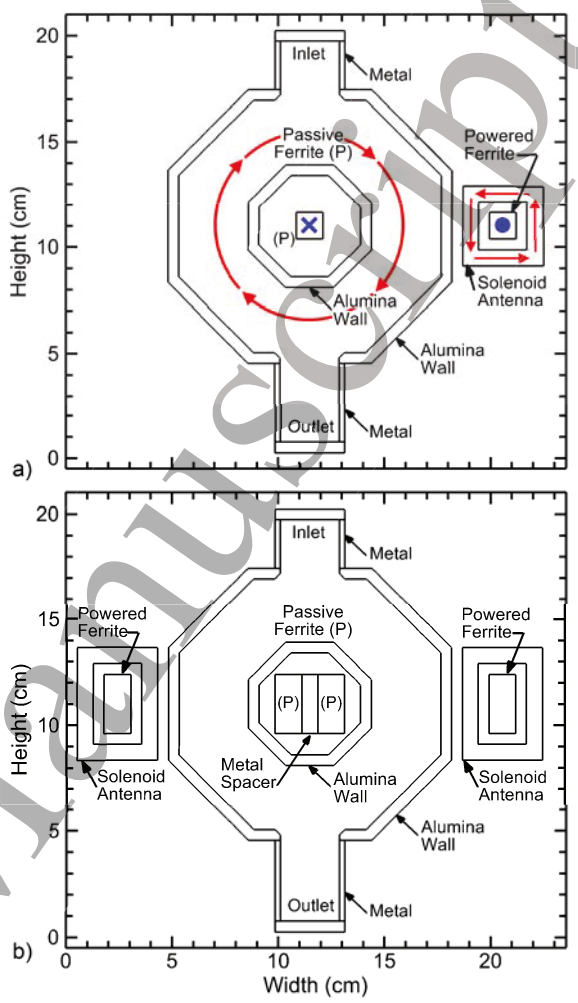


**Figure 1:** Schematic of the toroidal transformer coupled plasma (TTCP) sources employed in this study. a) Single ferrite core. The blue into and-out-of plane arrows represent directions of magnetic field. The red arrows represent direction of current or electric field. b) Dual ferrite cores.

In the first configuration (Fig.1a), RF current was supplied at 0.5 MHz to a single core by a 10-turn solenoidal current coil or antenna acting as the primary of the transformer. The current in Fig.1a flows counter-clockwise in the 2-dimensional plane of the calculation, producing a magnetic field through the ferrite pointing into the plane. The ferrite core is, conceptually, a closed loop oriented perpendicular to the simulation plane, passing through the primary coil and entering the center of the reactor. The *powered ferrite* is that portion of the core surrounded by the antenna. The *passive ferrite* is that portion of the core surrounded by the plasma. The purpose of the ferrite cores are to capture the magnetic field produced by the antenna and transmit that magnetic field to power the secondary turn of the transformer, which is the plasma. The transmitted magnetic field to the unpowered ferrite points perpendicularly out of the plane in Fig. 1a, with the

induced current through the plasma zone oriented in the clock-wise direction. In the second configuration (Fig. 1b) two independent 10 turn solenoid coils are coupled to the plasma through two independent transformer ferrite cores.

The square cross section for the single ferrite and rectangular cross sections for the dual ferrites are a consequence of limitations of the numerical mesh, which is rectilinear. That said, the majority of commercially available ferrite, closed loop cores do not have circular cross sections. The cross sections are typically rectangular due to fabrication challenges, and so the representations of the cores here reflect current practice. The rectangular cross sections of the cores then affect the symmetry of the induced electric fields generated by the magnetic fields carried by those cores.

The ferrite material has a relative permeability of $\mu_r = 100$, relative permittivity of $\varepsilon_r = 3.0$ and an electrical conductivity of $\sigma = 1 \times 10^{-7}/\Omega$-cm. The inner passive ferrite arms are inside a dielectric Macor housing. A grounded metal spacer placed between the two central ferrite materials is intended to guide electromagnetic field propagation outwards towards the plasma channels, rather than reconnecting between the two central ferrites. The plasma channels, lined by alumina coatings, are contained within a metallic shell. As a result, power is coupled from the antennae to the plasma entirely due to the ferrite generated electromagnetic fields.

The plasma chamber consists of a closed roughly circular path. The secondary loop of the transformer is the current conducted by the plasma. With a single ferrite core, the oscillating magnetic field through the passive ferrite produces an electric field in the plane of the simulation, oscillating in the azimuthal direction. With dual ferrite cores, the phases of the primary currents flowing through the antenna on the powered sides of the ferrites were chosen so that the sum of the induced electric fields generated by the passive ferrites are in phase and oscillate in the azimuthal direction.

The model used in this investigation was the 2-dimensional Hybrid Plasma Equipment Model (HPEM) [32]. The toroidal geometry and transformer power coupling was facilitated by adding a frequency domain solution and transformer surface current model into the existing HPEM framework to enable current loops in the (x,z) plane. In this implementation of the HPEM, a fluid treatment was used for the bulk electron, ion, and neutral species, and a kinetic treatment was used for secondary electrons. Bulk fluid heavy particle species fluxes were obtained using individual

continuity, momentum, and energy equations for each species with collisional mixing terms between species. This approach enables individual species to have unique temperatures and convective speeds. Thermodynamic properties of neutral species in mixtures were computed based on their individual Lennard-Jones 6-12 potentials and radii using the techniques discussed in Ref. [32] and [33]. Ion mobilities in mixtures were given by their total collision frequency with all other species, with diffusivities then given by the Einstein relation.

The temperatures of all solid materials were kept constant at 325 K assuming active cooling of the device. The inlet flow was given by the specified sccm with the flux being uniformly distributed across the inlet. Gas enters into the source with the temperature of the inlet material. The pressure was held constant on the surface of the pump port, with the outcome being a small pressure drop across the device. Slip boundary conditions for convective flow and jump boundary conditions for temperature were employed on all surfaces using a gas-solid accommodation coefficient of 0.8.

The mean bulk electron energy was obtained from a fluid based energy conservation equation [32]. Rate coefficients and transport coefficients were obtained from solutions of Boltzmann's equation for the bulk electron energy distributions using a two-term spherical harmonic expansion. These coefficients are stored in a table as a function of mean electron energy which is interpolated during the simulation. The table is updated as the gas composition evolves.

The rate of secondary electron emission from plasma-facing material surfaces varied in direct proportion to the incident heavy ion flux. An ion-induced secondary electron emission coefficient of 0.15 was assumed for alumina and metal plasma-facing surfaces [35]. Photon and electron induced secondary electrons were not considered in this work. Energy distributions of secondary electrons were explicitly computed using a Monte-Carlo method as described in Ref. [34]. The trajectories of secondary electrons, emitted with an initial energy of 3 eV, were tracked using Monte Carlo methods in the space and time varying electromagnetic and electrostatic fields. Secondary electrons interact with gas phase heavy particles using the same reaction mechanism as for bulk electrons while including electron-electron and electron-ion collisions. Statistics on the energy and locations of secondary electrons and electrons produced by ionizing collisions are recorded on every timestep weighted by the residence time of the electron in a given numerical cell. Secondary electrons falling below 2 eV were added to the bulk electron population through a source term in the bulk electron continuity equation. The distribution functions of the secondary

electrons are used to formulate source functions for electron impact processes that are added to continuity equations in the fluid portion of the model. With every call to the Monte Carlo simulation, $10^5$ particles were launched as secondary electrons.

Table 1: Species included in the reaction mechanism

| | |
|---|---|
| Charged Species | $e^-$, $Ar^+$, $Ar_2^+$, $F^+$, $F^-$, $F_2^+$, $N^+$, $N_2^+$, $NF_3^+$, $NF_2^+$, $NF^+$ |
| Neutral Species | Ar, Ar($1s_5$), Ar($1s_4$), Ar($1s_3$), Ar($1s_2$), Ar(4p), Ar(4d), $Ar_2$*, N, N*, F*, $F_2$*, $N_2$*, $N_2$**, $N_2$(v) |

Poisson's equation for the electrostatic potential was solved using a semi-implicit technique [32] with charge densities in the gas phase and on dielectric surfaces. All metal materials were grounded, including the outer boundary of the computational domain.

The species included in the model are in Table 1. The argon reaction mechanism is discussed in Ref. [36], and the $NF_3$ reaction mechanism is discussed in Refs. [37] and [38], with transport coefficients based on Ref. [39]. A brief description of the reaction mechanisms is given here. In this mechanism, F* (energetically F($3s^4P$)), $F_2$* (energetically $F_2(A\ ^3\Pi_u)$ and N* (energetically N($^2$D)) are lumped states including excitation to all higher lying states. $N_2$* is a lumped state energetically $N_2$(A) while also including excitation to $N_2(B^3\Pi)$, $N_2(W^3\Delta)$ and $N_2(B^3\Sigma)$. $N_2$** is similarly a lump state energetically $N_2(a'^1\Sigma)$ while also including excitation to all higher states. Equations 1 to 7 present examples of $NF_x$ electron impact reactions in the mechanism including (Eq. 1) elastic scattering, (Eq. 2) dissociative attachment, (Eq. 3) dissociative excitation, (Eq. 4) ionization, (Eq. 5) dissociative ionization, (Eq. 6) dissociative recombination and (Eq. 7) dissociative ion-ion neutralization.

$$e + NF_x \rightarrow NF_x + e \quad (1)$$

$$e + NF_x \rightarrow NF_{x-1} + F^- \quad (2)$$

$$e + NF_x \rightarrow NF_{x-1} + F + e \quad (3)$$

$$e + NF_x \rightarrow NF_x^+ + e + e \quad (4)$$

$$e + NF_x \rightarrow NF_{x-n}^+ + nF + e + e \quad (5)$$

$$e + NF_x^+ \rightarrow NF_{x-1} + F \quad (6)$$

$$F^- + NF_x^+ \rightarrow NF_{x-1} + F + F \quad (7)$$

Rate coefficients for electron impact reactions were calculated from electron energy distributions obtained from stationary solutions of Boltzmann's equation [32]. Heavy particle mixing and cascade process between excited species were also included with rate coefficients obtained from Refs. [40–43] for argon and Refs. [39,40] for $NF_x$ species. In computing argon ion transport coefficients and the resulting ion temperatures, the momentum transfer cross-sections were reduced inversely proportional to temperature above 1000 K to capture the fall off in heavy particle interaction cross-sections at high ion velocities [44]. Gas heating sources included Joule heating, elastic collisions with electrons, changes in enthalpy due to gas phase reactions, Franck-Condon heating due to dissociative electron impact and recombination, and ion-ion neutralization processes. Conductive heat exchange occurs between the gas phase and walls, and convective heat exchange occurs at the inlet and outlet.

**II.A Transformer Power Coupling Model**

Addressing the toroidal remote plasma sources with current loops in the x-z plane required modification of the existing HPEM framework. A solution of the electric field frequency domain wave equation in the Electromagnetics Module (EMM) was implemented to enable modelling of lateral (x) and axially (z) orientated currents and electric fields in a Cartesian plane. A transformer coupling model was also developed to facilitate coupling of the primary winding induced out-of-plane magnetic field ($B_{cT\theta}$) between the powered and unpowered arms of the ferrite materials, and to compute the resulting induced secondary winding (x,z) electric field components. Electric fields in the (x,z) plane are produced using a Successive Over Relaxation (SOR) solution to the frequency domain wave equation,

$$-\nabla\left(\frac{1}{\mu(\vec{r})}\nabla\cdot\vec{E}_T(\vec{r},t)\right) + \nabla\cdot\left(\frac{1}{\mu(\vec{r})}\nabla\vec{E}_T(\vec{r},t)\right) = \frac{\partial^2\left(\varepsilon(\vec{r})\vec{E}_T(\vec{r},t)\right)}{\partial t^2} + \frac{\partial\left(\vec{J}_p(\vec{r},t)+\vec{J}_a(\vec{r},t)+\vec{J}_t(\vec{r},t)\right)}{\partial t} \quad (8)$$

where, $\vec{E}_T$ is the electric field vector resulting from the toroidal transformer, and $\epsilon$ and $\mu$ are the material dependent permittivity and permeability. The current components include: $J_p$ the plasma current density, $J_a$ the antenna current density, and $J_t$ the effective transformer current density, discussed below. In the frequency domain,

$$\vec{E}_T(\vec{r},t) = \vec{E}_{To}(\vec{r})\exp\left(i\left(\omega t + \vec{\phi}_E(\vec{r})\right)\right) = \vec{E}_{cTo}(\vec{r})\exp(i\omega t) \quad (9)$$

$$\vec{J}_a(\vec{r},t) = \frac{\vec{I}_o(\vec{r})}{\lambda_S d}\exp(i\left(\omega t + \vec{\phi}_a(\vec{r})\right) = \frac{\vec{I}_{co}(\vec{r})}{\lambda_S d}\exp(i\omega t) \quad (10)$$

$$\vec{J}_p(\vec{r},t) = \bar{\bar{\sigma}}\cdot\vec{E}(\vec{r},t), \quad (11)$$

where $\vec{E}_{To}(\vec{r})$ is the real amplitude of the electric field, $\vec{\phi}_E(\vec{r})$ is its phase with the vector notation indicating a unique phase for each component of the electric field and $\vec{E}_{cTo}(\vec{r})$ is the complex amplitude including phase $\vec{\phi}_E(\vec{r})$ (the phasor), where the subscript *c* generally denotes a complex quantity. $\vec{I}_o(\vec{r})$ is the direction amplitude of the antenna current where $\lambda_S$ is the skin depth of the wave into the metal of the antenna and d is the depth (thickness) of the antenna. $\bar{\bar{\sigma}}$ is the tensor conductivity having contributions from electrons and ions which, in the absence of an applied static magnetic field, has only diagonal elements.

The transformer current density is $\vec{J}_i(\vec{r},\phi)$ defined only in *unpowered* ferrite materials which serve as the secondary winding of the transformer circuit. Computationally, in 2-dimensions, the spatial locations of the ferrite material serving as the primary winding of the transformer are mapped 1-to-1 to locations in the secondary winding. This mapping requires the shape of the primary and secondary ferrites to be the same. The transformer ferrites carry only a non-zero azimuthal magnetic field ($B\theta$). $B_{c\theta}(\vec{r})$ in the powered, primary ferrite is computed from,

$$\nabla\times\vec{E}_T = -\frac{\partial\vec{B}_T}{\partial t}, \quad \vec{B}_T(\vec{r},t) = \vec{B}_{cTo}(\vec{r})\exp(i\omega t), \quad B_{cT\theta}(\vec{r}) = \frac{i}{\omega}\left[\frac{dE_{cTz}(\vec{r})}{dx} - \frac{dE_{cTx}(\vec{r})}{dz}\right]. \quad (12)$$

The magnetic field in the secondary, passive ferrite is $B_{cT\theta}(\vec{r}') = B_{cT\theta}(\vec{r})\exp(-i\pi)$ where $\vec{r}'$ is the secondary 1-to-1 mapped location of the primary location $\vec{r}$. With the magnetic field oriented into the plane in the primary ferrite and out of the plane for the secondary ferrite, there is a 180° phase shift in the secondary winding. The current density in the secondary ferrite is then,

$$\vec{J}_{cTx}(\vec{r}) = \frac{-1}{\mu}\left(\nabla\times\vec{B}_{cT\theta}(\vec{r})\right) - i\omega\varepsilon\vec{E}_{cTx}(\vec{r}), \quad (13)$$

$$\vec{J}_{cTz}(\vec{r}) = \frac{1}{\mu}\left(\nabla\times\vec{B}_{cT\theta}(\vec{r})\right) - i\omega\varepsilon\vec{E}_{cTz}(\vec{r}). \quad (14)$$

Substituting for $B_{cT\theta}$ from Eq. 12,

$$J_{cTx}(\vec{r}) = \frac{-1}{\mu(\vec{r})}\left(\frac{d^2E_{cTz}(\vec{r})}{dxdz} - \frac{d^2E_{cTx}(\vec{r})}{dz^2}\right) - i\omega\varepsilon(\vec{r})E_{cTx}(\vec{r}) \quad (15)$$

$$J_{cTz}(\vec{r}) = \frac{1}{\mu(\vec{r})}\left(\frac{d^2E_{cTz}(\vec{r})}{dx^2} - \frac{d^2E_{cTx}(\vec{r})}{dzdx}\right) - i\omega\varepsilon(\vec{r})E_{cTz}(\vec{r}). \quad (16)$$

Equations 15 and 16 describe the external current density components that would be required to produce an electric field of the strength and distributions experienced at the powered ferrite material surface. Including the transformer current densities (Eqs. 15 and 16) in Eq. 8 for the solution of $\vec{E}_T$ results in the generation of a time-varying electric field adjacent to the unpowered arm of the ferrite in proportion to the electric fields induced by the antenna at the powered arm of the ferrite.

This formulation implicitly assumes no magnetic flux leakage from the ferrites, and no induction of internal eddy currents, maintaining a purely azimuthal (perpendicular to the computational plane) magnetic field vector throughout the simulation domain. Given the low-field coupling (< 1000 G) and low driving current frequency (< 1 MHz), ignoring flux leakage and eddy currents should have few consequences. Commercially available transformer cores are typically constructed of laminar sheets of ferrite material, inhibiting internal eddy currents.

In previous implementations of the 2-dimensional HPEM, the inductively coupled electric fields were produced by antenna currents perpendicular to the plane of the simulation, which in the absence of an externally applied magnetic field, produces only a perpendicular component of the electric field, $E_\theta$. This component of the electric field is perpendicular to the plane in which plasma transport is computed in the Fluid, Kinetics and Poisson Module (FKPM) in which Poisson's equation is also solved. As a result, in the FKPM $E_\theta$ appears only as a heating term in the electron energy equation and does not directly affect plasma transport in the (r,z) for cylindrical or (x,z) for Cartesian planes. When simulating toroidal plasma sources, the inductively coupled electric fields, $E_x$ and $E_z$, are in the same plane as plasma transport is computed, and so must be accounted for in the FKPM. The following method was used.

The HPEM uses time-slicing techniques in which the solution for electromagnetic fields from the EMM are held constant while computing transport in the FKPM; and plasma properties produced in the FKPM are held constant when computing inductively coupled fields in the EMM. In the FKPM, ion transport is computed using continuity, momentum, and energy equations. The

transformer produced $\vec{E}_T(\vec{r},t)$ are directly included in the momentum and energy equations using their time dependent form,

$$\vec{E}_T(\vec{r},t) = \left|\vec{E}_{cT}(\vec{r})\right| \cos\left(\omega t + \vec{\phi}_E(\vec{r})\right) \tag{17}$$

The consequences of these fields are then naturally accounted for in the resulting ion momenta. Electron transport is addressed using a drift diffusion formulation. $\vec{E}_T(\vec{r},t)$ was added to the electrostatic electric field, $\vec{E}_S(\vec{r},t) = -\nabla\Phi_S$, where $\Phi_S$ is the electrostatic potential produced by solution of Poisson's equation. The electron flux is then

$$\vec{\phi}_e(\vec{r},t) = -D_e(\vec{r},t)\nabla n_e - \mu_e(\vec{r},t)\left[\vec{E}_S(\vec{r},t) + \vec{E}_T(\vec{r},t)\right] \tag{18}$$

where $D_e$ and $\mu_e$ are the free electron diffusion and mobility of electrons. Any charge separation that might occur due to drift resulting from $\vec{E}_T(\vec{r},t)$ is compensated by the value of $\vec{E}_S(\vec{r},t)$ produced by Poisson's equation. In the time-slicing methodology used in the HPEM, there is no real-time feedback to regulate the value of $\vec{E}_T(\vec{r},t)$. Since the drift motion of electrons is proportional to the sum of $\vec{E}_S(\vec{r},t)$ and $\vec{E}_T(\vec{r},t)$, this needed feedback is provided by regulation of $\vec{E}_S(\vec{r},t)$ so that their sum provides the needed current continuity without there being charge separation. This is achieved by adding the change in electron density due to drift driven by $\vec{E}_T(\vec{r},t)$ to an effective diffusion term in the semi-implicit solution of Poisson's equation for $\Phi_S$,

$$\begin{aligned} -\nabla\cdot\varepsilon\nabla\Phi_S(t+\Delta t) &= \rho(t) + \Delta t\frac{d\rho(t)}{dt} = \\ &= \rho(t) - \Delta t\sum_j \nabla\cdot q_j\phi_j(t) + \nabla\cdot q_e\mu_e n_e(t)\nabla\Phi_S(t+\Delta t) + \nabla\cdot q_e D_e\nabla n_e(t) - \nabla\cdot q_e\mu_e n_e(t)E_T(t) \end{aligned} \tag{19}$$

where $\phi_j(\vec{r},t)$ is the flux of ion j provided by the momentum equation for that species.

## III. TTCP Sustained in Argon

### A. Single Ferrite Core

Plasma properties ($E_T$, electron flux and electron temperature) for the single core TTCP sustained in Ar are shown in Fig. 2a. The conditions are an outlet pressure of 1.0 Torr with a flow rate of 500 sccm and 1.0 kW power deposition at a driving frequency of 0.5 MHz. The values are

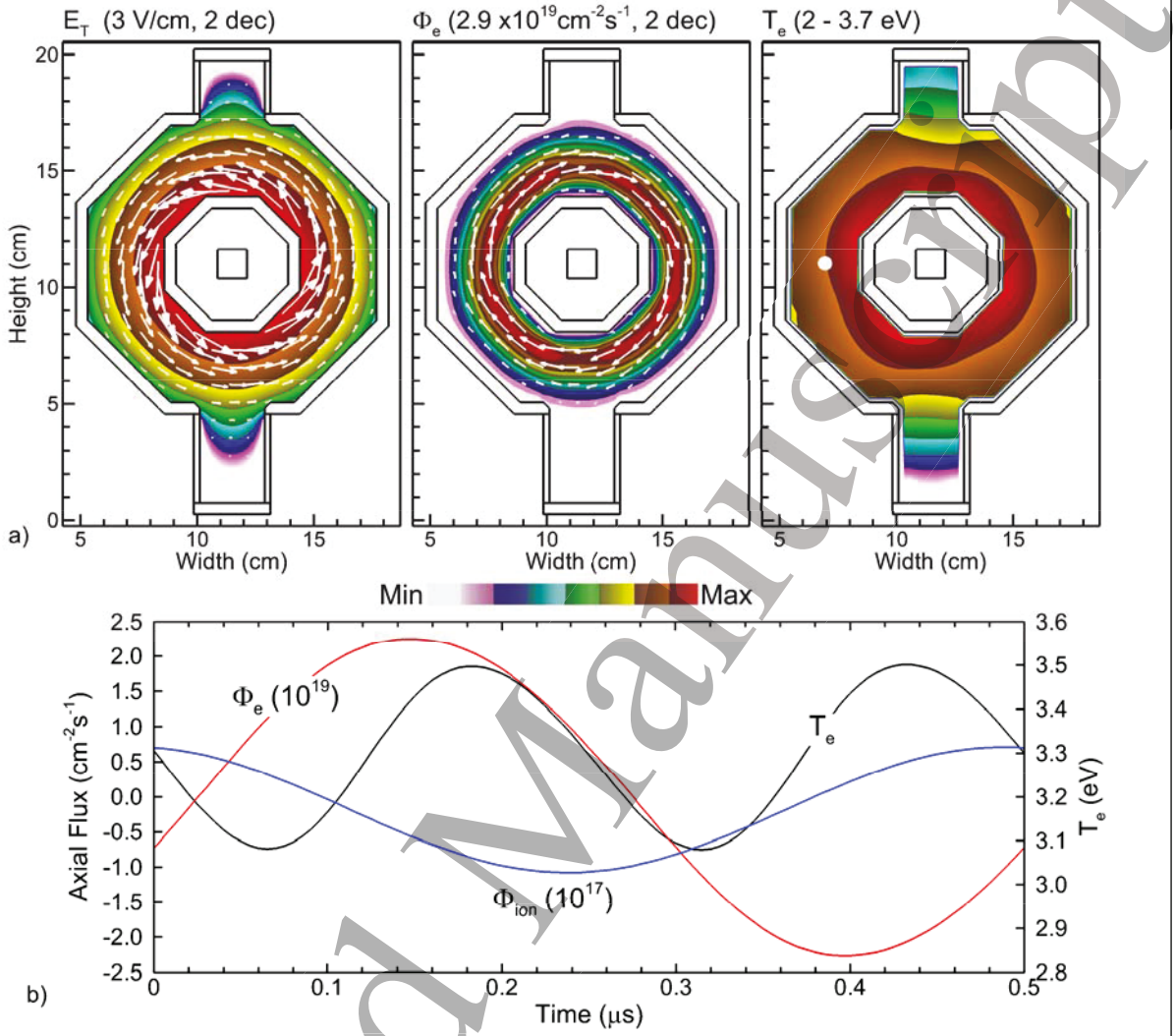


**Figure 2:** Plasma properties for the single core TTCP operating in 1 Torr Ar flowing at 500 sccm with 1 kW power deposition. a) Azimuthal electric field $E_T$, electron flux $\Phi_e$, and electron temperature $T_e$ for phase $\theta = 180°$ when the induced electric field $E_T$ is oriented counter-clockwise. The flood contours show the magnitude of $E_T$, electron flux $\Phi_e$, while the arrows show vector direction and magnitude. The maximum value or range of values plotted are noted at the top of each image, with "dec" indicating the number of decades for log-plots. b) Electron temperature, electron flux and ion flux during a single cycle at the location shown by the white dot in the flood contour of $T_e$.

shown at RF phase $\theta = 180°$ for which the induced field has a maximum in the counter-clockwise orientation. In Fig. 2 (and following figures), values are shown using flood contours for which quantities N are plotted in proportion to $\log_{10}(N)$. For example, an image plotted using a 2-dec log scale has contours ranging from a minimum of $\log_{10}(N/100)$ to a maximum of $\log_{10}(N)$.

With the single ferrite core having a square cross section, the induced electric field $E_T$ will be oriented and oscillate in the azimuthal direction. The magnitude of $E_T$, in the absence of absorption, would decrease with increasing radial distance from the center of the core. For the single

core RPS, the magnitude of $E_T$ is 3 V/cm at the inner wall of the plasma channel and 0.4 V/cm at the outer wall, corresponding to E/N = 32 Td (1 Td = $10^{-17}$ V-cm$^2$) at the inner wall and 5 Td at the outer wall. The plasma conductivity at the middle of the channel is 2.7 S/cm, which provides a skin depth of 4.3 cm, on the order of the channel width of 3.3 cm. With the width of the core (1.3 cm) being small compared to the inner width of the plasma channel (5.8 cm) the importance of the non-circular cross section of the core is lessened and the vector $E_T$ maps out a circular path. Consequently, the vector electron flux also maps out a circular closed loop path. The majority of current carried in the secondary loop of the TTCP represented by the plasma is conduction current.

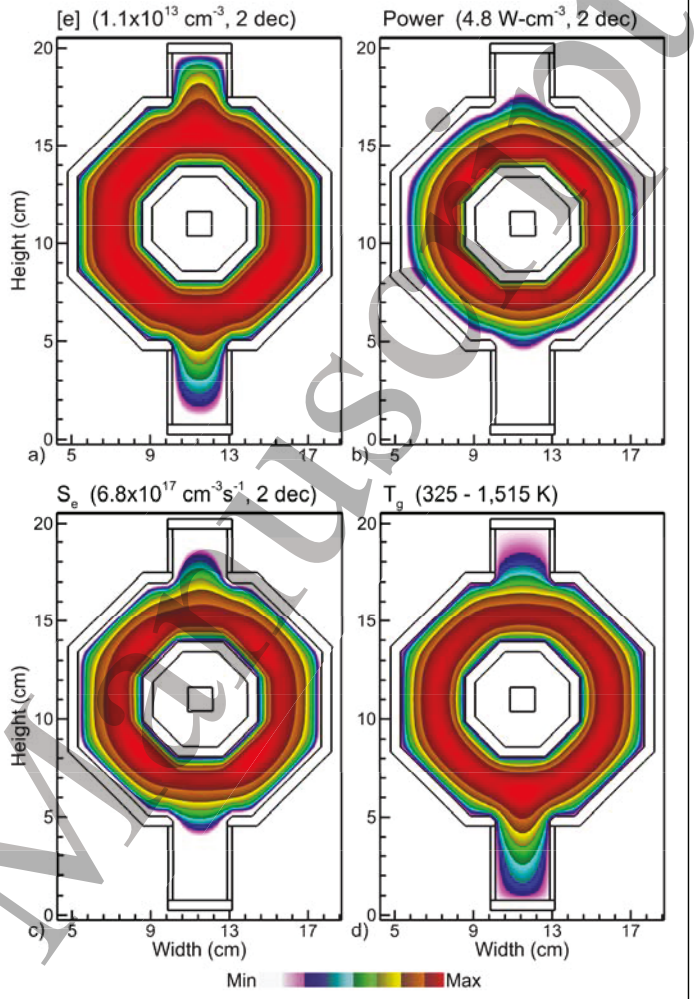


**Figure 3:** Plasma properties for the single ferrite core configuration operating in argon averaged over the RF cycle. a) Electron density, b) power deposition, c) electron impact ionization source and d) average gas temperature. Operating conditions are 1.0 kW, 0.5 MHz, 1.0 Torr. The maximum value or range of values plotted are noted at the top of each image, with "dec" indicating the number of

The non-circular geometry of the device does have consequences, as shown by the electron temperature. $T_e$ is maximum at 3.7 eV at the inner wall of the plasma channel where $E_T$ is largest, decreasing to 3.3 eV at the outer wall. However, with the heating rate of the electron temperature being proportional to $E_T$, the small changes in $E_T$ resulting from the non-circular core and inner wall produce some azimuthal asymmetries in $T_e$.

With the electron momentum transfer collision frequency at mid-channel being $9.4 \times 10^8$ s$^{-1}$, and $E_T$ oscillating at $5 \times 10^5$ s$^{-1}$, there is intra-cycle oscillation in charged particle fluxes and electron temperature. The axial (vertical) component of electron flux and ion flux, and the electron

temperature are shown in Fig. 2b during the RF cycle at the location denoted by the white-dot in Fig. 2a. The axial electron flux oscillates with an amplitude of $2.2 \times 10^{19}$ $cm^{-2}s^{-1}$ (3.5 $A/cm^2$) compared to its random thermal flux of $1 \times 10^{22}$ $cm^{-2}s^{-1}$. The oscillation represents a fractional modulation of about 0.2% of the random flux, but sufficient to carry the induced current. The axial flux of $Ar^+$ oscillates with an amplitude of $1.1 \times 10^{17}$ $cm^{-2}s^{-1}$. The electron temperature oscillates with an amplitude of 0.22 eV about its mean value of 3.3 eV.

Plasma properties (electron density, power deposition, electron impact ionization source and gas temperature) averaged over the RF cycle are shown in Fig. 3. The mid-channel electron density is $1.1 \times 10^{13}$ $cm^{-3}$, balanced dominantly by $Ar^+$. (The $Ar_2^+$ density is $3.4 \times 10^9$ $cm^{-3}$.) This electron density is produced by a maximum power deposition of 4.8 $W/cm^3$, slanted towards the inner wall where $E_T$ is maximum. Ionization by bulk electrons has a maximum value of $6.8 \times 10^{17}$ $cm^{-3}$ $s^{-1}$. The plasma potential is positive with respect to the walls by only 15-20 V. Acceleration of secondary electrons by this potential does not produce particularly energetic particles, resulting in the ionization source by secondary electron being about $10^{-3}$ that of the bulk electrons. The quantities that are particularly sensitive to the local amplitude of $E_T$, power deposition and ionization source, do show some azimuth variation resulting from the non-circular cross section of the ferrite and the inner housing. For example, power deposition has an azimuthal non-uniformity of about 20% (maximum vs. minimum). With electrons having non-local transport, the uniformity of the electron density is greater, with only 8% azimuthal variation.

The maximum mid-channel gas temperature is 1,515 K, resulting from the temperature of the plasma-facing surfaces being held constant at 325 K. This is, to some degree, an artificial constraint based on the assumption of active cooling of the device. The gas dynamics, heating and resulting rarefaction do impact the plasma parameters. Ambient temperature gas is flowed into the top of the plasma source and hot gas is exhausted at the bottom, which produces an axial gradient and is responsible for some portion of the azimuthal (here, top-to-bottom) asymmetry in plasma properties. At a pressure of 1 Torr, large pressure gradients are difficult to sustain. With an outlet boundary condition of 1 Torr, the inlet pressure is 1.03 Torr.

## B. Dual Ferrite Core

When operating a TTCP at high power levels, it may not be practical to deliver the entire power through a single ferrite core. In those cases, applying power through two (or more) ferrite

cores is a potential solution. In using a dual ferrite core configuration, it is difficult to maintain the ideal azimuthal symmetry of the induced electric field $E_T$ that would result from a magnetic field oscillating through a small diameter wire. From a practical perspective, most ferrite cores in closed loops have rectangular cross sections. To maximize the area of the cores (and so reduce their specific power loading) while passing two cores through the central opening of the plasma channels, each core has a large aspect ratio, here 2.8 cm tall × 1.3 cm wide or an aspect ratio of 2. This configuration also results in the vertical faces of the cores being physically closer to the plasma channel than the horizontal faces. These geometrical constraints then result in azimuthal asymmetries in $E_T$ and the plasma properties that follow.

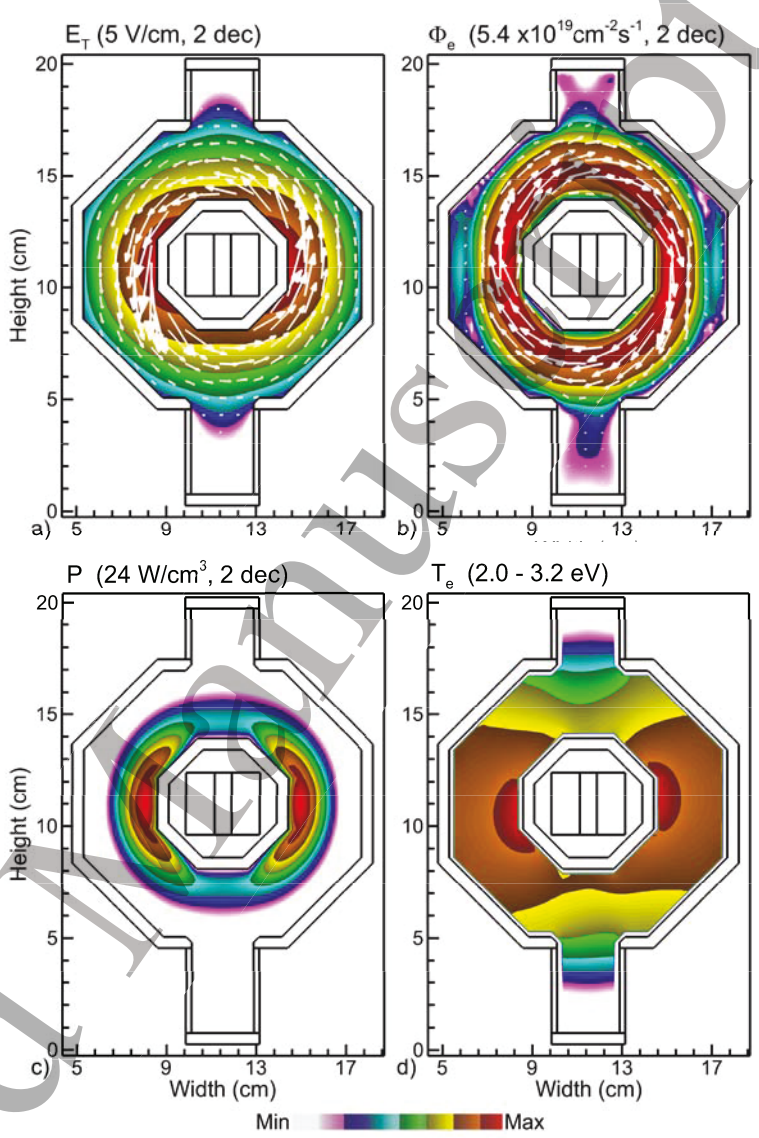


**Figure 4:** Plasma properties for dual ferrite core TTCP sustained in argon for phase $\theta = 180°$ when the induced electric field $E_T$ is oriented counter-clockwise. (a) Absolute magnitude of $E_T$ with vector electric fields, (b) electron flux magnitude with vector electron flux vectors, c) power deposition and d) electron temperature. Operating conditions are 1.0 kW, 0.5 MHz, 1.0 Torr. The maximum value or range of values plotted are noted at the top of each image, with "dec" indicating the number of decades for log-plots.

Plasma properties for a dual ferrite core TTCP sustained in argon for phase $\theta = 180°$ when the induced electric field $E_T$ is oriented counter-clockwise are shown in Fig. 4. The quantities plotted are a) absolute magnitude of $E_T$ with vector electric fields, b) electron flux magnitude with vector electron flux, c) power deposition and d) electron temperature. Operating conditions are 1.0 kW, 0.5 MHz, 1.0 Torr. The

directions of the currents in the primary loops powering the ferrites are chosen so that the individual $E_T$ produced by each ferrite are in phase. The $E_T$ shown in Fig. 4 results from the in-phase sum of the electric fields induced by the oscillating magnetic fields guided by the two side-by-side ferrite cores in the center of the device. The magnitude of $E_T$ is maximum along the inner vertical wall at 5 V/cm, compared to 2 V/cm along the top horizontal wall.

The orientation of $E_T$, shown by the white arrows, forms a closed loop around the central block, resulting in alternating clockwise and counter-clockwise acceleration of charged particles. The electron flux has a maximum value of $5.4 \times 10^{19}$ $cm^{-2}s^{-1}$ or 8.6 $A\text{-}cm^{-2}$ and aligned counter-clockwise and anti-parallel to $E_T$ the induced electric field. In the absence of $E_T$, electric fields are dominated by the ambipolar electric fields which point from the center of the plasma towards boundaries, with electron motion being diffusion dominated towards surfaces. With the superposition of $E_T$, electron motion is instantaneously dominated by the oscillating azimuthal motion. Averaged over an RF cycle, the oscillating azimuthal motion and current density averages to zero, leaving ambipolar diffusion towards walls as the dominate net flux of electrons and ions.

Although the direction of the conduction current density, indicated by the arrows in Fig. 4b, forms a closed loop, the conduction current density is itself not continuous. The electron flux and conduction current density are maximum along the equator of the device in the axial direction where the electron density is also maximum (discussed below), which results in the oval-shape loop. The required current continuity is maintained by displacement current in the horizonal direction on the top and bottom of the loop. This offset between conduction and displacement current is an artifact of the topology of this design. With the side-by-side pair of ferrite cores having rectangular shapes, the maximum $E_T$, power deposition and conduction current density are along the internal vertical surfaces of the device.

The division of azimuthal current around the loop between conduction and displacement currents does not necessarily benefit nor detract from the performance of the TTCP. In the extreme where current flows only by conduction current in one portion of the loop and only by displacement current in another portion of the loop, the TTCP would resemble a dielectric barrier discharge (DBD). As with a DBD, the details of proportion between conduction and displacement current affects the impedance of the device which must be accounted for in matching to the power source.

The power deposition (maximum of 24.0 $Wcm^{-3}$) and electron temperature (maximum 3.2 eV ) at $\theta = 180°$, are shown in Fig. 4c and 4d. The total RF power density scales as: $P = \sigma E^2$, and

so is maximum at the intersection of the highest plasma conductivity (on-axis in the channel) and the highest electric field strength (adjacent to the inner walls). The electron temperature $T_e$ should, in principle, be maximum at the maximum power deposition. There is, however, an azimuthal symmetry that results from oscillations in the plasma potential, discussed below.

The cycle averaged electron density, electron impact ionization source, Ar($1s_5$) density and gas temperature are shown in Fig. 5. The electron density is maximum in the center of the vertical channels at $2.6 \times 10^{13}$ cm$^{-3}$ reflecting the maximum in power deposition. The electron density reduces to $1.2 \times 10^{13}$ cm$^{-3}$ and $1.0 \times 10^{13}$ cm$^{-3}$ in the upper and lower horizontal channels. The reduction in the lower horizontal channel is due to the higher neutral gas temperature and lower gas density that enables higher diffusion losses. The electron density does not significantly vary over the RF cycle, as distinct from the electron flux. The electron density rapidly decays upwards into the inlet and downwards into the outlet tubes. Wall losses dominate this reduction in density as the fractional contribution

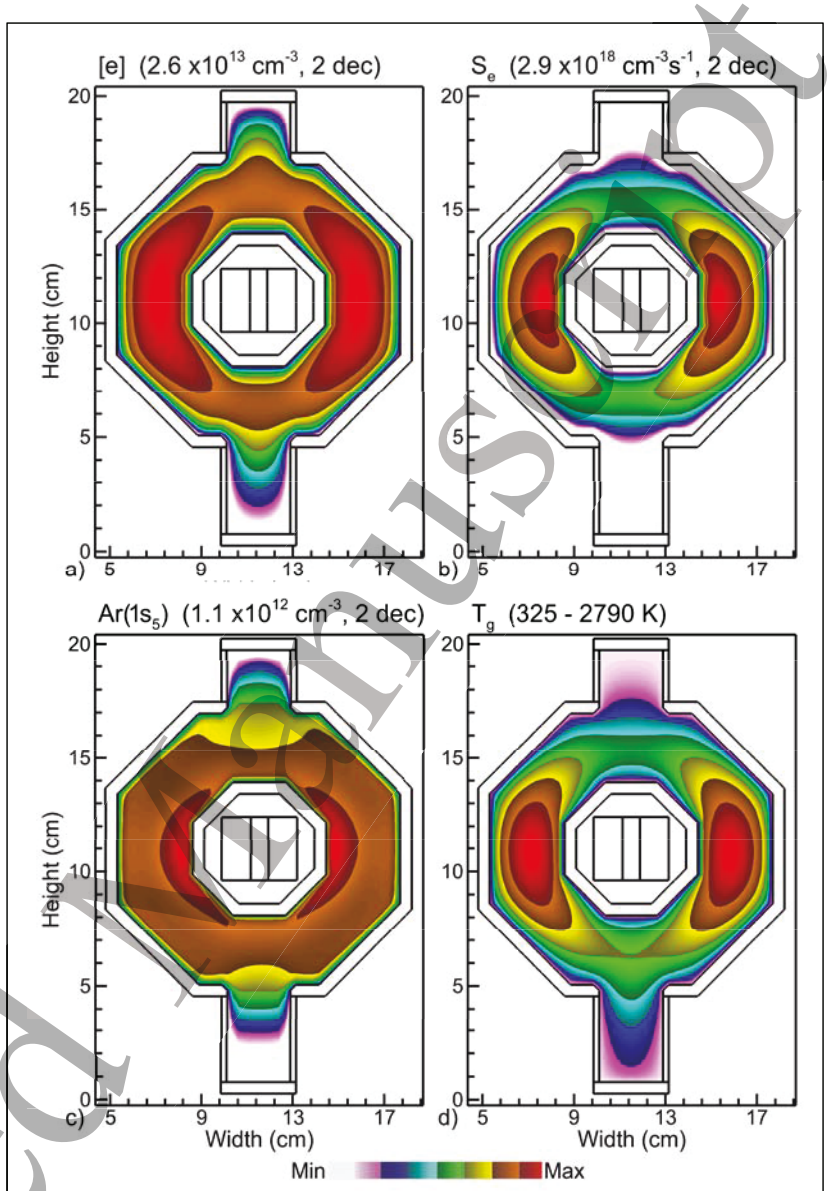


**Figure 5:** Plasma properties for the dual ferrite core TTCP sustained in argon averaged over the RF cycle. (a) electron density, (b) bulk electron impact ionization source, (c) Ar($1s_5$) density and (d) average gas temperature. Operating conditions are 1.0 kW, 0.5 MHz, 1.0 Torr. The maximum value or range of values plotted are noted at the top of each image, with "dec" indicating the number of decades for log-plots.

to dissociative recombination to $Ar_2^+$ is small, while the plasma potential gradient inhibits net electron fluxes out of the source.

The bulk ionization rate is a maximum of $2.9 \times 10^{18}$ cm$^{-3}$s$^{-1}$ sustained by an electron temperature of 3.2 eV (Fig. 4d). At a pressure of 1.0 Torr (with gas heating) the electron collision frequency is $\approx 10^9$ s$^{-1}$ and the electron mean free path is between 0.5 cm and 1.0 cm (horizontal and vertical channels, respectively). As a result, electron transport is largely dominated by local fields. Maxima in electron density, temperature, and ionization source correlate with the maximum in RF power density. The plasma is predominately sustained through direct electron impact ionization of ground state argon and multistep ionization of the Ar($1s_5$) and Ar($1s_4$) states. The density of Ar($1s_5$), shown in Fig. 5c, is maximum along the inner walls at $1.1 \times 10^{12}$ cm$^{-3}$. Multistep ionization of the Ar($1s_3$) and Ar($1s_2$) states contribute approximately 10% of the total bulk $Ar^+$ ionization rate.

In contrast to the single ferrite configuration, the asymmetry in power deposition also produces an asymmetry in gas heating, shown in Fig. 5d. The gas temperature is maximum mid-channel at 2,790 K, significantly higher than the single ferrite device due to the locally higher power deposition. With cool gas being injected at the top and hot gas being pumped out at the bottom, additional asymmetries are introduced. As with the single-ferrite configuration, there is only a moderate pressure gradient across the device. The inlet pressure is 1.05 Torr for an outlet pressure of 1.0 Torr. The pressure gradient is nearly twice that of the single-ferrite source due to the higher local gas temperature, which requires a larger body force from the pressure gradient to maintain the flow rate.

The electron flux, plasma potential and electron temperature are shown in Fig. 6 as a function of phase during the RF cycle, where $\theta = 0°$ is the phase of maximum clockwise azimuthal electric field and $\theta = 180°$ is the phase of maximum counterclockwise azimuthal electric field. Properties for the phases $\theta = 180°$ - $360°$ are symmetric to $\theta = 0°$ - $180°$. The electron flux, $\Phi_e$, varies from a maximum of $4.2 \times 10^{19}$ cm$^{-2}$ s$^{-1}$ (6.7 A/cm$^2$) at $\theta = 0°$ oriented dominantly in the azimuth direction, decreasing to essentially zero in the azimuthal direction at $\theta = 90°$, before changing direction and rising back to $\Phi_e = 4.2 \times 10^{19}$ cm$^{-2}$ s$^{-1}$ at $\theta = 180°$ dominantly in the azimuthal direction in the counter-clockwise direction. The argon ion flux $\Phi_{Ar+}$ (not shown) does not instantaneously respond to the applied RF fields at 500 kHz. Instead $\Phi_{Ar+}$ is predominately orientated towards the walls and remains approximately constant throughout the RF phase cycle. The

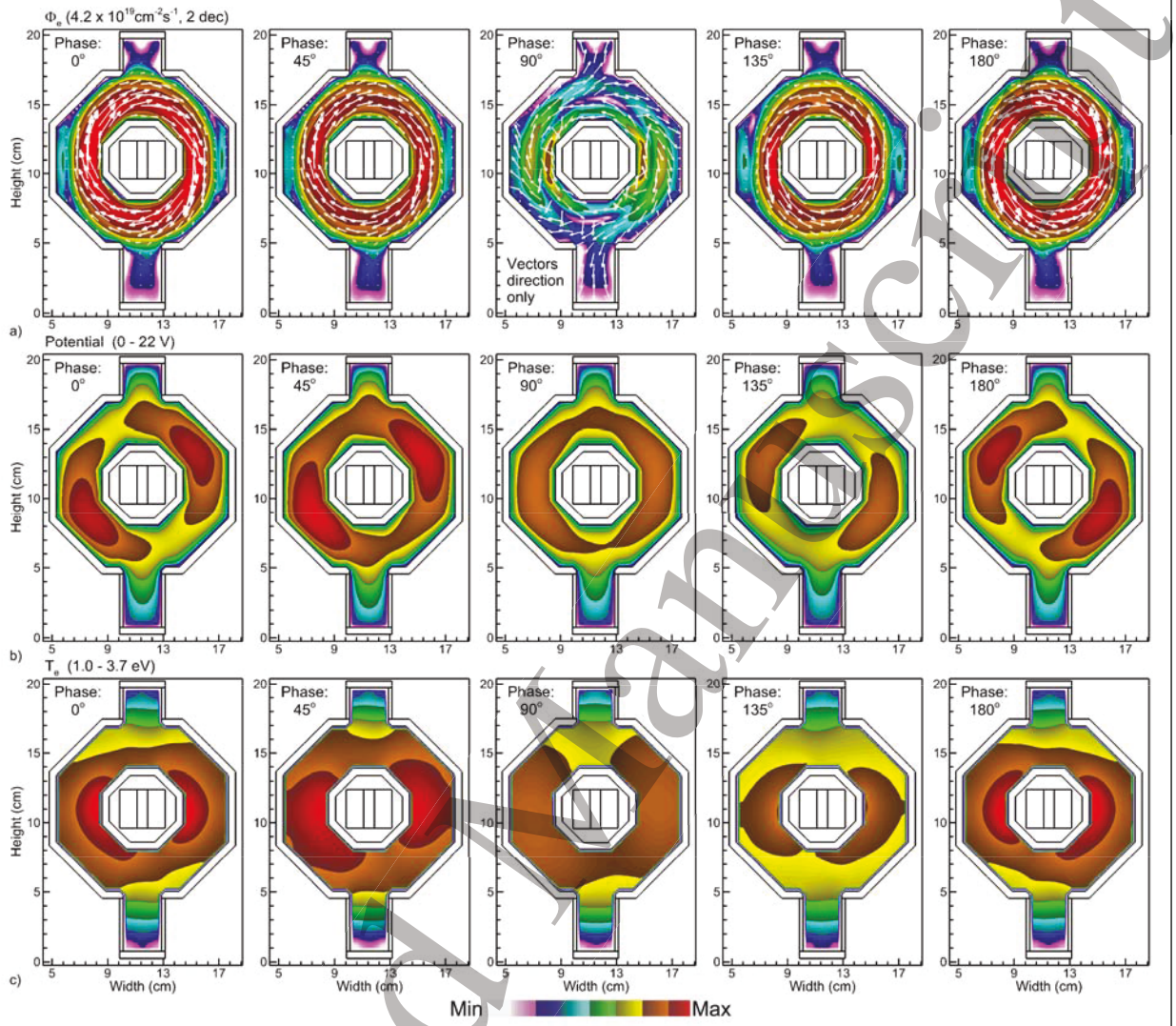


**Figure 6:** Plasma properties for the dual core TTCP sustained in argon for phase $\theta = 0°$ to 180°, where $\theta = 0°$ is when the induced electric field $E_T$ is oriented at its maximum clockwise. a) Absolute magnitude electron flux and vector flux. (The flux vectors for $\theta = 90°$ show direction only.) b) Electric potential and c) electron temperature. The conditions are 1.0 kW, 0.5 MHz, 1.0 Torr. The maximum value or range of values plotted are noted at the top of each image, with "dec" indicating the number of decades for log-plots.

maximum in $\Phi_{Ar^+}$ is $2.1 \times 10^{18}$ cm$^{-2}$ s$^{-1}$ incident upon the inboard walls within the vertical channels. The ion flux to the dielectric walls must be balanced, averaged over the RF cycle, by the electron flux. This balance is achieved. However the azimuthal electron flux in the (counter direction) of $E_T$ is large in comparison. At $\theta = 90°$, the azimuthal $E_T$ passes through zero magnitude and the electric fields in the plasma channel are dominated by ambipolar electric fields. At that phase, the magnitude of the electron flux is reduced by an order of magnitude, while its direction is largely towards boundaries. For example, in Fig. 6a for electron flux at $\theta = 90°$, the inner band

of electron flux is directed towards the inner walls, and the outer band is directed towards the outer walls.

The phase-resolved plasma potential, shown in Fig. 6b, exhibits an azimuthal rotation. This azimuthal oscillation in the plasma potential results from the azimuthal oscillation of $E_T$ and the electron density not being azimuthally symmetric. The electron flux rapidly responds to the acceleration resulting from oscillation of $E_T$ while the ions are slowly accelerated in the opposite direction by $E_T$. The azimuthal gradients in electron density then result in space charge separation. This space charge is produced along the azimuthal flux lines of the electrons. The response of the system to the induced space charge is to generate azimuthal components of the electrostatic field to limit further space charge separation. These confining azimuthal components of the electric field then produce local maxima in and azimuthal oscillation the plasma potential. At $\theta = 90°$ when the charge separation driven by $E_T$ is a minimum, the plasma potential is symmetric across the midplane.

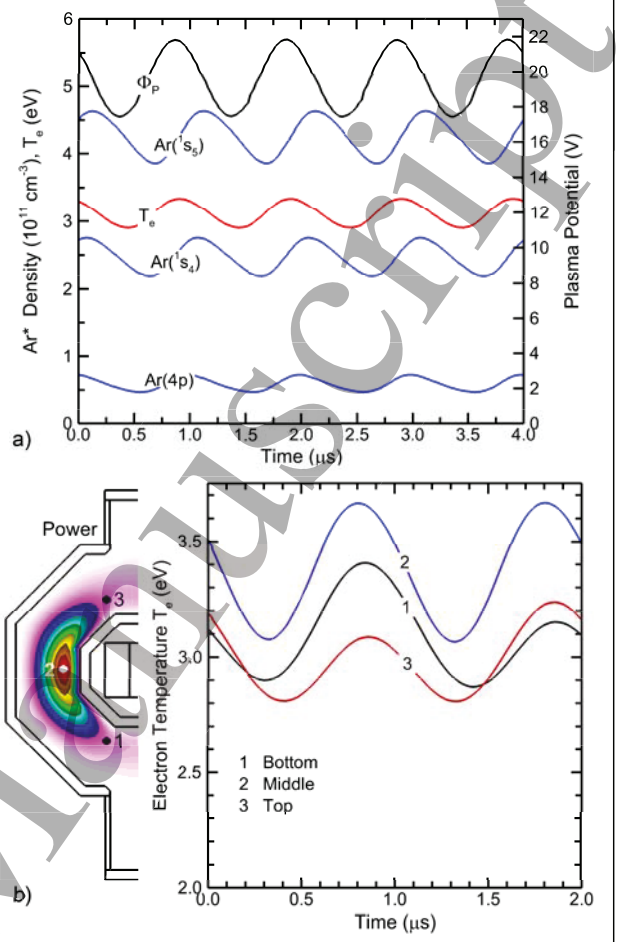


**Figure 7:** Plasma properties as a function of time. a) Plasma potential, argon excited state density and electron temperature averaged over the plasma region for 2 RF cycles. b) Electron temperature at three locations indicated by the schematic showing power deposition. Operating conditions are 1.0 kW, 0.5 MHz, 1.0 Torr of argon.

A perfectly symmetric azimuthal geometry would be produced by a circular secondary arm of the transformer, and circular inner and outer walls of the RPS. These conditions would then produce an azimuthally symmetric $E_T$, ionization source, electron and ion densities and plasma potential. The electron flux would uniformly increase, decrease and reverse direction in the azimuthal direction which, in the absence of azimuthal gradients, negates the need for a compensating electrostatic electric field to confine space charge. Even with nominally circular geometries for the secondary arm of the transformer and walls, there are invariably gas inlets and outlets that

break the azimuthal symmetry. This break in symmetry produces azimuthal gradients in plasma properties, as shown by the single-ferrite TTCP discussed earlier.

The electron temperature as a function of phase is shown in Fig. 6c. Similar to the plasma potential, there is an azimuthal oscillation in the electron temperature which mirrors that of the plasma potential while the RF heating source does not exhibit this oscillation. The oscillation results in part from convection of electrons in the $E_T$ electric field and in part by extraction of electron energy in producing the confining electrostatic fields that counter $E_T$.

With the electron collision frequency producing a time between collisions being a small fraction of the RF period (2 μs), there is some equilibration of the plasma properties with the oscillation of $E_T$. For example, electron temperature, argon excited state density and plasma potential are shown in Fig. 7a averaged over the plasma regions during two RF cycles. Excited states have densities of low-to-mid $10^{11}$ $cm^{-3}$ which oscillate with ±10% over the RF cycle. In principle, the oscillation in plasma properties should be symmetric over any given cycle. That symmetry is broken for excited state densities due to the spatial inhomogeneity in electron temperature. $T_e$ at three locations during an RF cycle is shown in Fig.

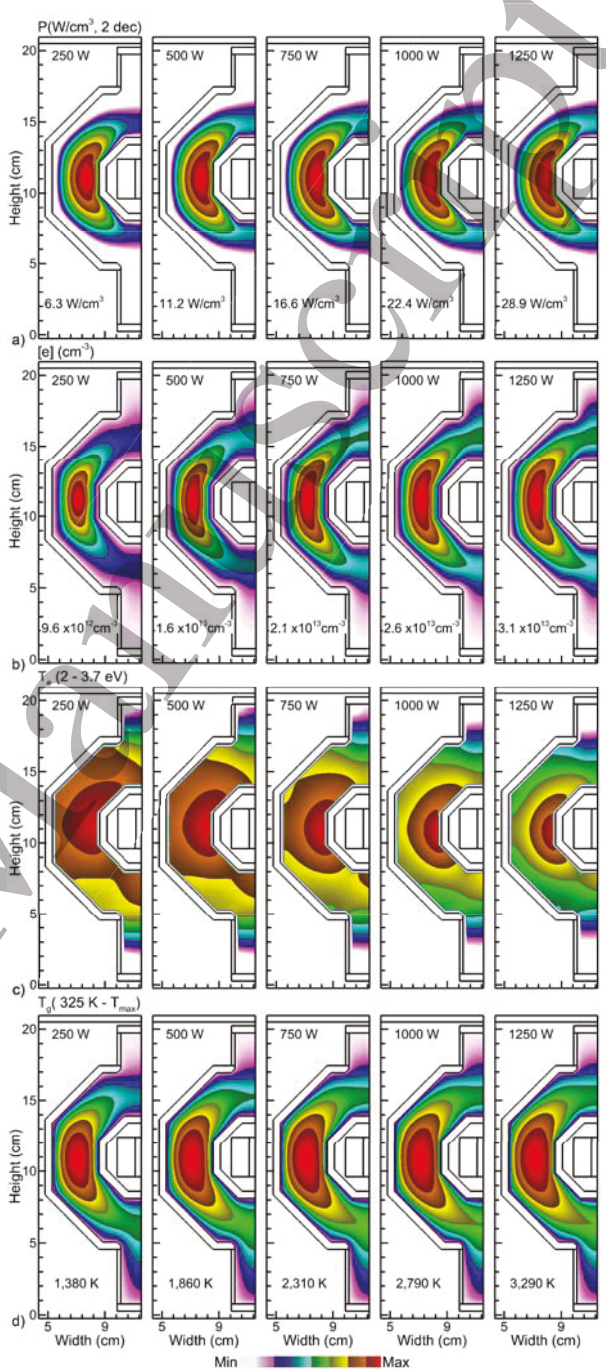


**Figure 8:** Plasma properties averaged over the RF cycle as a function of power deposition (250 W to 1250 W) in argon. a) Power deposition, b) electron density, c) electron temperature and gas temperature. Operating conditions are 0.5 MHz, 1.0 Torr. The maximum values plotted are noted at the top of the sequence or in the image, with "dec" indicating the number of decades for log-plots.

7b. (The schematic at left shows power deposition averaged over the RF cycle.) $T_e$ is maximum and oscillates with the largest amplitude at the maximum in power deposition. The location at the top of the reactor has a lower $T_e$ than its mirrored location at the bottom. This asymmetry results from gas heating and gas flow, which produces a plume of hotter, less dense gas lower in the reactor.

Plasma properties (power deposition, electron density, electron temperature and gas temperature) are shown in Fig. 8 for operating in argon at 1 Torr for a total power deposition between 250 W and 1250 W. Over this power range, the maximum electron density increases from $9.6 \times 10^{12}$ $cm^{-3}$ to $3.1 \times 10^{13}$ $cm^{-13}$, a factor of 3, while the total electron inventory (spatial integral of electron density) scales nearly linearly with power deposition. The less than linear increase in maximum electron density while the inventory scales nearly linearly with power deposition results from the more spatially extended power deposition at high power. The greater gas heating at the higher power results in more severe rarefaction and a broader distribution of plasma density. The maximum gas temperature increases from 1,380 K to 3,290 K, with the gas density at the peak of power deposition rarefying from $7.1 \times 10^{15}$ $cm^{-3}$ to $2.9 \times 10^{15}$ $cm^{-3}$.

Bai et al. spectroscopically measured gas temperatures in a similar TTCP device sustained in argon by observing the spectra of an added trace amount of $N_2$ [20]. Their method resolved gas temperature as a function of position in a plane perpendicular to the gas flow and averaged axially along the flow direction. For an average power deposition of 4.5 $W/cm^3$ at 1 Torr, the maximum gas temperature was 1560 K. The data in Fig. 8 was processed to best replicate the measurement technique used by Bai et al, and we predict a temperature of 2,055 K. The experimental measurements were made for at least twice the equivalent flowrate, which may account for the lower gas temperature.

The electron temperature becomes more highly confined as the power deposition increases. This confinement in $T_e$ results from several factors. From 250 W to 1250 W, the conductivity at peak power deposition increases from 2.2 S/cm to 4.4 S/cm, producing a decrease in skin depth from 4.8 cm to 3.0 cm. This decrease in skin depth produces more local electron heating. The decrease in gas density produces an increase in E/N (based on $E_T$) from 33 Td at 250 W to 104 Td at 1250 W with $E_T$ increasing from 2.3 V/cm to 3.1 V/cm. With electron heating rates scaling as $E_T^2$, heating again becomes more local.

## IV. TTCP Sustained in Ar/$NF_3$ Mixtures

The use of RPSs in microelectronics fabrication is typically as a source of halogen radicals (e.g., F, Cl) or oxygen atoms for isotropic etching and chamber cleaning. The source gases can be highly attaching, which significantly affect the ionization dynamics and macroscopic discharge properties of the RPS. A widely used gas for F atom production is nitrogen-trifluoride, $NF_3$. F atom production in $NF_3$ containing plasmas is efficient due to the large dissociative attachment, excitation, and recombination rate coefficients for electron interactions with $NF_3$.

With $NF_3$ being a thermally attaching gas, it is experimentally difficult to initiate the plasma in the purely inductive electric field produced by the transformer. The E/N that can be produced in the device is not sufficient to break down pure $NF_3$. In commercial operation, this quandary is addressed by the discharge being initiated in a flow of argon. Once the plasma is ignited, the flow is progressively diluted with $NF_3$ while maintaining power until the flow consists of only $NF_3$. Computationally, igniting the plasma in pure $NF_3$ is also challenging for the same reasons as observed experimentally. Unrealistic currents in the primary would be required to produce a large enough E/N through pure inductively coupling to initiate a plasma in $NF_3$. The Ar/$NF_3$ discharges discussed here were therefore ignited in pure argon

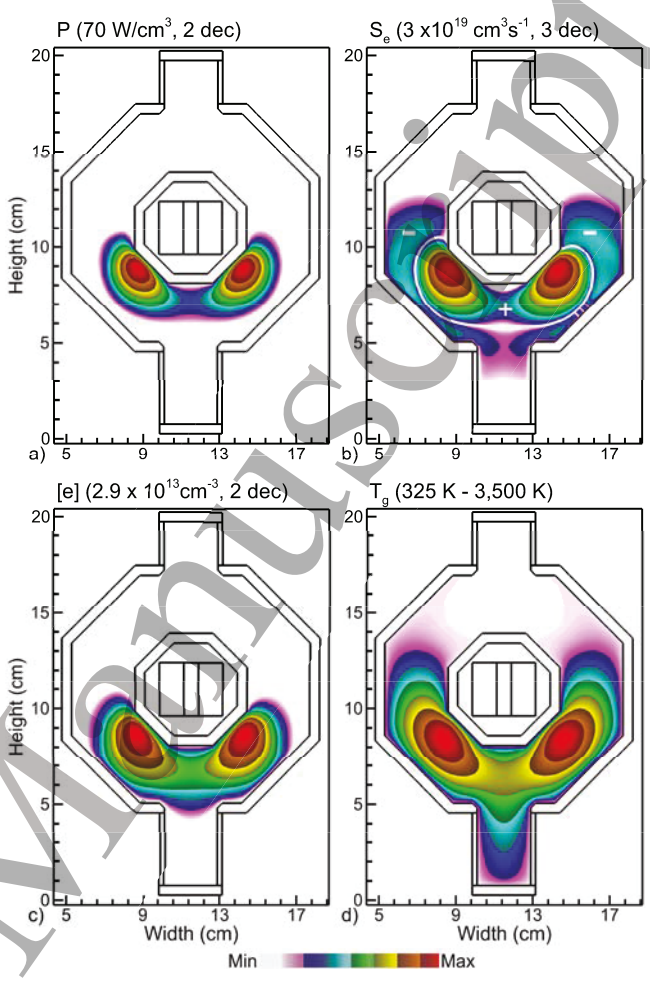


**Figure 9:** Plasma properties averaged over the RF cycle for the TTCP sustained in pure $NF_3$ for 1 kW, 1 Torr, 0.5 MHz, 500 sccm operation. a) Power deposition, b) electron impact ionization source, c) electron density and d) gas temperature. The maximum value or range of values plotted are noted at the top of each image, with "dec" indicating the number of decades for log-plots. In the plot for ionization source, the absolute value of the source is plotted with the white line separating positive and negative sources . The regions labelled "+" are net positive sources of electrons where ionization dominates. The regions labelled "-" are net negative sources where attachment and recombination dominate.

into which an Ar/$NF_3$ mixture was flowed, mimicking startup practices in commercial devices.

We first discuss plasma properties of the RPS operating in pure $NF_3$ using the dual ferrite-core geometry shown in Fig. 1b for a power deposition of 1 kW and flowrate of 500 sccm. The outlet pressure boundary condition is 1 Torr. Plasma properties (power deposition, electron impact ionization source, electron density and gas temperature) averaged over the RF cycle are shown in Fig.9. In the image for ionization source, the absolute value of the source is plotted. The regions labelled "+" are net positive source of electrons where ionization dominates. The regions labelled "-" are net negative sources where attachment and recombination dominate. The resulting densities of $NF_3$, $NF_2$, NF, F, N and $N_2$ are shown in Fig. 10.

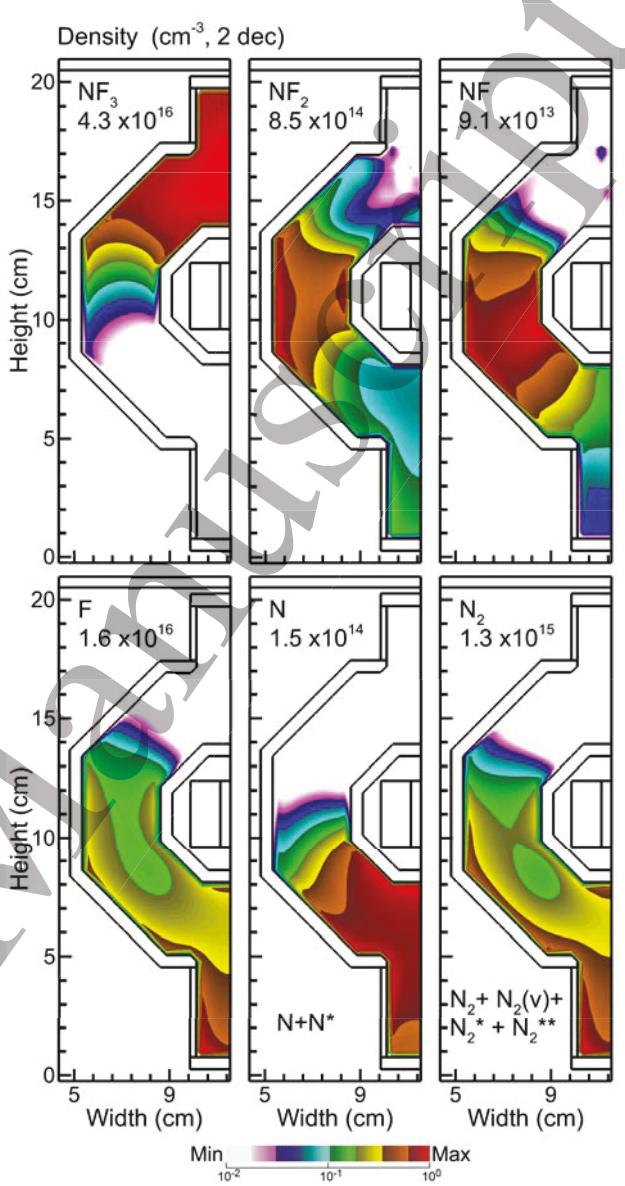


**Figure 10:** Neutral densities produced in the TTCP sustained in pure $NF_3$ for 1 kW, 1 Torr, 0.5 MHz, 500 sccm operation - $NF_3$, $NF_2$, NF, F, N and $N_2$. The plots for N and $N_2$ include excited states of those species. Densities are plotted on a 2-decade log-scale with the maximum value indicated in each frame.

The mode of operating the TTCP is to adjust the current flowing through the primary windings of the transformer to deliver the specified power in the secondary current loop represented by the plasma. The resulting $E_T$ will generate a plasma that delivers the specified power preferentially into those regions having the lowest impedance (and highest conductivity). The flow of $NF_3$ into the reactor produces a highly attaching environment. The gas is essentially pure $NF_3$ in the top of the reactor prior to there being any dissociation of the feedstock gas. With power deposition, gas heating and rarefaction occurring lower in the reactor, the gas

density of highly attaching gas is larger at the top of the reactor. This higher density produces a lower E/N for a given electric field. The end result is that the plasma cannot be sustained in the upper portion of the reactor. This inability to sustain the plasma in the upper portion of the reactor is exacerbated by $NF_3$ being a thermally attaching gas. In the upper region of the reactor which has a low electron temperature, dissociative attachment dominates over the negligible rate of ionization. The plasma is dominantly sustained in those regions of the reactor where the $NF_x$ density decreases to the point that attachment no longer dominates over ionization.

The extinction of the upstream electron population results from electrons diffusing upwards that are lost to dissociative attachment to the $NF_3$ feed gas and $NF_x$ fragments. Dissociative attachment to $NF_3$ is a thermal process having essentially no threshold energy and so attachment is rapid for even low energy electrons. The electron density is largely confined to the region of positive electron impact source (Fig. 9b) where the electron temperature is high enough (maximum $T_e = 4.1$ eV) to sustain net positive ionization. With the electron energy relaxation length being 0.5 – 1 cm, the system rapidly transitions to net attachment and recombination within a few cm of the maximum of net positive ionization. The net positive ionization source has two distinct maxima of $3 \times 10^{19}$ cm$^{-3}$s$^{-1}$ aligning with the location of highest electron density. The region of net positive ionization is surrounded by a halo of net attachment and dissociative recombination having a maximum loss of $4.2 \times 10^{17}$ cm$^{-3}$s$^{-1}$. The electron source is net negative both upstream and downstream of the maximum in power deposition, sustained by a small net electron current ($2 \times 10^{18}$ cm$^{-2}$s$^{-1}$, 0.3 A/cm$^2$) from the region of net positive ionization. With the gas flow being laminar, there is little mixing of the dissociated gas in the lower portion of the device and the non-dissociated gas in the upper portion of the device. So the transition from attachment dominated to net ionization can be rapid.

While the total volume integrated electron inventory is reduced when operating in $NF_3$ compared to pure argon, the maximum electron density is similar to the argon-only base case at $2.9 \times 10^{13}$ cm$^{-3}$. With the specific power deposition (eV/collision) being larger for the molecular gas compared to argon, the total 1 kW of power deposition in $NF_3$ can be sustained with a lower total inventory of electrons. While the plasma density, and hence plasma conduction current loop, is discontinuous in the $NF_3$ discharge, there is toroidal displacement current flowing through the upstream region such that $\oint \mu\left(\vec{j} + \varepsilon d\vec{E}_T/dt\right)\cdot d\vec{l}$ is conserved within each closed toroidal loop as with the pure argon case.

For the same power deposition that produced a maximum gas temperature of 2,790 K in argon, the maximum gas temperature in $NF_3$ is 3,500 K. The higher gas temperature results from the more localized power deposition (maximum 70 W/cm$^3$) and more localized electron impact dissociative processes (attachment, electronic excitation, recombination) that produce gas heating through Franck-Condon relaxation that produces hot fragments. The gas temperature is high enough that there is a significant contribution of thermal dissociation of $NF_3$. For example, at the top boundary between the positive and negative electron sources, the gas temperature is 2,900 K, the electron temperature is 3.8 eV and the electron density is $1.4 \times 10^{12}$ cm$^{-3}$. For these conditions, approximately 25% of the dissociation of $NF_3$ is due to heavy particle thermal processes (e.g., $NF_3 + M \rightarrow NF_2 + F + M$, with M being a third body.) For a similar TTCP source operating in $NF_3$, Gangoli et al. [4] used global modeling to determine that dissociation of $NF_3$ was dominated by non-thermal electron impact for gas temperatures less than 2000 K at electron temperatures of 4-5 eV, and dominated by thermal processes at higher temperatures. Li et al [24] measured $NF_3$ dissociation of about 95% for a similar device. The operating conditions of that device (pressure, flow rate and power) resulted in a comparable specific energy deposition (eV/molecule) as in this investigation.

Fluorine negative ions (anions), produced by dissociative attachment to $NF_x$ and $F_2$, are the dominant negatively charged heavy species. At the top boundary between the positive and negative ionization sources, the $F^-$ density is $2 \times 10^{12}$ cm$^{-3}$ and the electron density is $1 \times 10^{12}$ cm$^{-3}$. Moving towards the top of the device, the electron density rapidly decays due to dissociative attachment to $NF_3$. For example, in the middle of the vertical channel (2 cm higher in the reactor) the $F^-$ density is $1.2 \times 10^{12}$ cm$^{-3}$ and the electron density is $5 \times 10^{10}$ cm$^{-3}$. In the top of the device where the electron density is negligible, the $F^-$ density is $1.7 \times 10^{10}$ cm$^{-3}$ balanced by a nearly equal density of $NF_3^+$ forming an ion-ion plasma. These species are not produced locally but rather diffuse from the bulk plasma under influence of a weak ambipolar electric field that accounts for the difference in diffusivities of $F^-$ and $NF_3^+$.

Depletion of the upstream electron density significantly reduces the plasma conductivity. The maximum conductivity is 4 S/cm at the location of maximum electron density, decreasing to 1-10 μS/cm upstream. As the upstream conductivity reduces, the RF power is coupled into a smaller total volume, co-located with the downstream plasma density.

Dissociation of $NF_3$ produces $NF_2$, NF, N, and F neutral fragments, which appear as axial

layers within the source as the $NF_3$ flows from the inlet and undergoes sequential dissociation processes, as shown in Fig. 10. $NF_3$ is rapidly dissociated by electron dissociative excitation and attachment upon entering the source with its density decreasing over two orders of magnitude from $3.2 \times 10^{16}$ cm$^{-3}$ at the inlet to the boundary of the plasma zone (height = 10 cm). Dissociation of $NF_3$ produces maximum densities of $NF_2$ of $6 \times 10^{14}$ cm$^{-3}$ (height = 11 cm). Dissociation of $NF_2$ in turn produces maximum NF densities of $7 \times 10^{13}$ cm$^{-3}$ (height = 9 cm). The NF is finally dissociated to produce, N atoms. Surface recombination of $NF_2^+$ and $NF^+$ produce sources of $NF_2$ and NF at the walls which produces local maxima in the densities of $NF_2$ and NF. The inlet flux of $NF_3$ is $2.5 \times 10^{19}$ cm$^{-2}$s$^{-1}$. The combined $NF_x$ (x = 1,2,3) at flux at the outlet is $1.8 \times 10^{18}$ cm$^{-2}$s$^{-1}$, representing about 92% fractional dissociation $NF_x$.

Atomic nitrogen is produced following the electron impact dissociation of NF, which energetically favors the production of N + F$^-$. The branching of electron impact dissociation of $NF_2$ to N + 2F makes a small contribution. The maximum atomic nitrogen density is of $1.5 \times 10^{14}$ cm$^{-3}$ in the outlet tube. Molecular nitrogen is produced by recombination of N on the walls reaching a maximum density of $1.3 \times 10^{15}$ cm$^{-3}$ in the outlet of the tube, of which about one-third is vibrationally excited. Once $N_2$ is formed, it is a terminal species in terms of producing N atoms as the rate of electron impact dissociation of $N_2$ is low.

The F atom density increases throughout the source from the inlet to the outlet as all dissociative processes involving $NF_x$ produce F atoms. The maximum density of F at the outlet is $1.2 \times 10^{16}$ cm$^{-3}$ with a flux of $6 \times 10^{19}$ cm$^{-2}$s$^{-1}$, representing the largest product leaving the reactor. F is produced by the successive dissociation of $NF_3$ to $NF_2$ to NF to N + F. $F_2$ is produced by 3-body recombination of F while surface recombination of F producing $F_2$ occurs throughout the source. The flux of $F_2$ at the outlet is $5 \times 10^{18}$ cm$^{-2}$s$^{-1}$, about 10% that of the outlet F flux.

The confined plasma resulting from the flow of highly attaching $NF_3$ and the azimuthally driven electron currents resulting from the oscillating $E_T$ produce vortex motion of the electrons while maintaining charge balance. When averaged over the RF cycle, the flux of electrons to the dielectric surfaces of the plasma channel must equal the sum of the flux of positive ions. (The flux of negative ions is small in comparison.)

The RF averaged density of positive ions and flux vectors are shown in Fig. 11a. The corresponding values for electrons are also shown in Fig. 11 for phases of 0° ($E_T$ oriented fully clockwise), 90°($E_T$ =0) and 180° ($E_T$ oriented fully counter-clockwise). The electron fluxes must

simultaneously satisfy the need to match the ion fluxes to surfaces (averaged over the RF cycle) while carrying the azimuthal toroidal plasma current. The ambipolar component of the electron flux that matches the ion flux points radially outwards from the maximum in electron and ion density. The toroidal current component of the electron flux is maximum near the inner wall, while alternating in the azimuthal direction. The vector sum of these requirements results in vortex-like electron flux vectors. For the 0° phase, the vortex is counter-clockwise and at 180° the vortex is clockwise. For the 90° phase when $E_T$ =0, the electron fluxes are dominated by their ambipolar component and point towards surfaces.

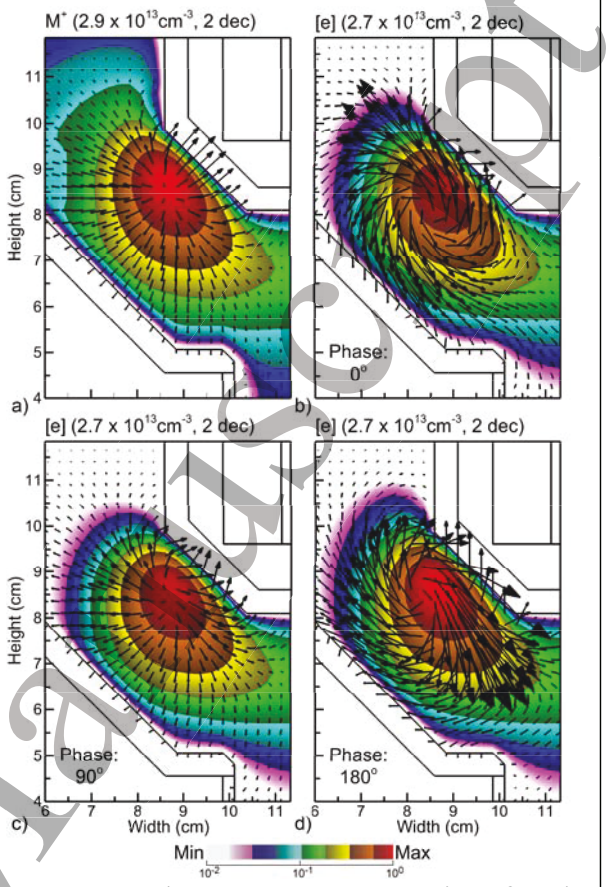


**Figure 11:** Plasma transport properties of positive ions and electrons for the TTCP operating in $NF_3$. a) Density of the sum of all positive ions with ion flux vectors. The electron density and electron flux vectors are are shown for phase $\theta$ = a) 0°, b) 90° and c) 180°. Densities are plotted on a 2-decade log-scale with the maximum value indicated in each frame. Operating conditions are 1.0 kW, 0.5 MHz, 1.0 Torr.

The confinement of the plasma by the flow of highly attaching $NF_3$ is a function of the $NF_3$ flow rate. The electron density and electron impact ionization source are shown in Fig. 12 for $Ar/NF_3$ inlet mole fractions of $Ar/NF_3$ = 100/0 (pure Ar) to $Ar/NF_3$=0/100 (pure $NF_3$). The conditions are 1 kW, 500 sccm and 1 Torr outlet pressure. With inlet mole fractions of only a few percent, the plasma in the upper portion of the reactor is extinguished, producing the confined plasma downstream. With $Ar/NF_3$ = 95/5, the confined plasma is nominally centered at the maximum of $E_T$, as with the pure argon, though extending further downstream into the fully dissociated $NF_3$ than extending upstream into the incoming flow of $NF_3$. The ionization source has distinct regions of net positive and net negative electron production. With progressively larger $NF_3$ inlet mole fractions, the confined plasma decreases in spatial extent and shifts lower in the reactor. The plasma stabilizes where a critically large fraction of the $NF_x$ has been dissociated, and rates of attachment have diminished. The maximum plasma density and ionization source both increase in

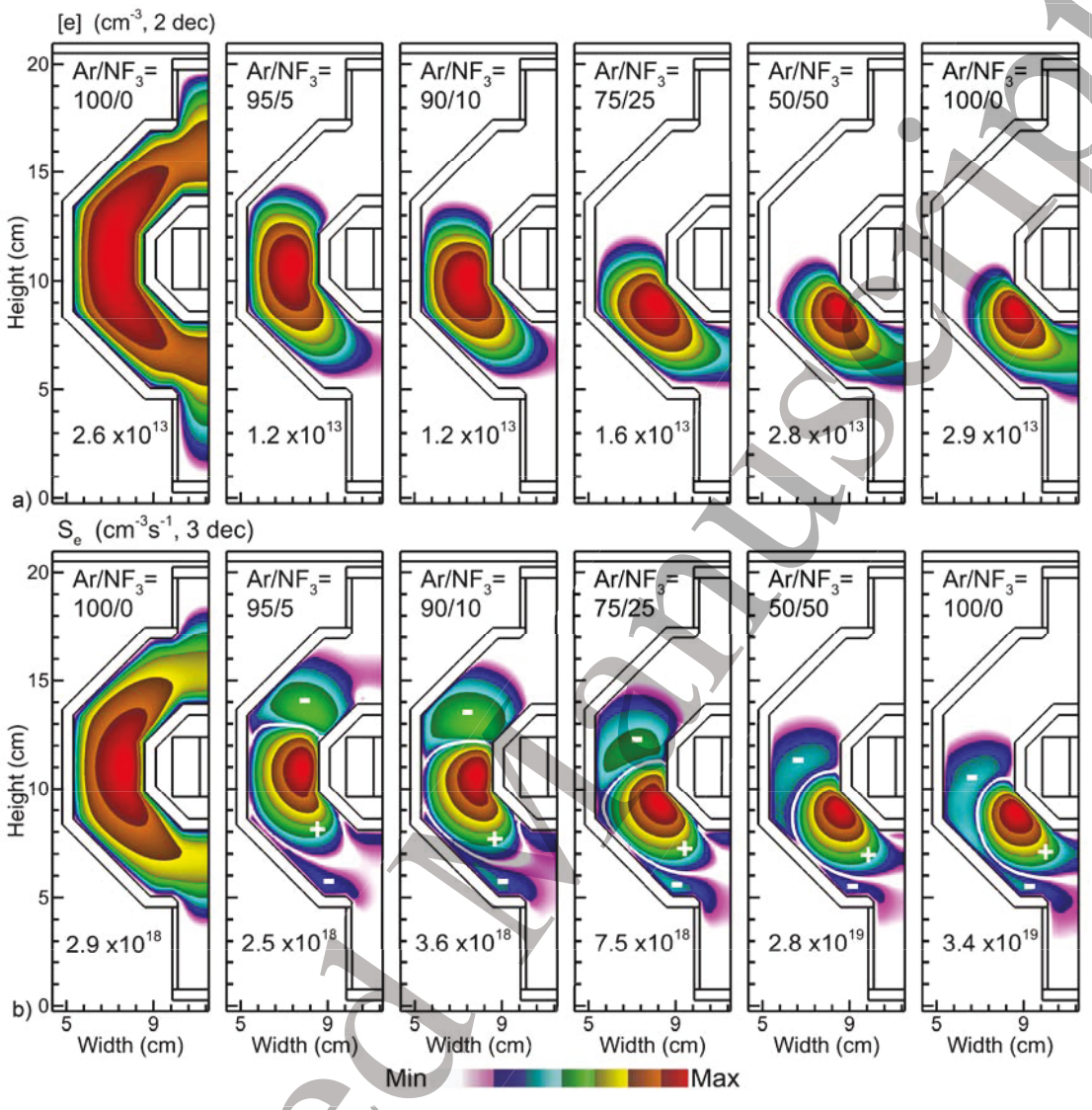


**Figure 12:** Plasma properties averaged over the RF cycle for the TTCP operating in $Ar/NF_3$ gas mixtures ranging from pure Ar to pure $NF_3$. a) Electron density and b) electron impact ionization source. The images are log-plots (2-decades for electron density and 3-decades for ionization source) with the maximum value noted in each frame. In the plot for ionization source, the absolute value of the source is plotted with the white line separating positive and negative sources. The regions labelled "+" are net positive sources of electrons where ionization dominates. The regions labelled "-" are net negative sources where attachment and recombination dominate. Operating conditions are 1 kW, 0.5 MHz and 1 Torr.

the more confined plasma with an increase in $NF_3$ fraction so that the total power deposition remains 1 kW.

## V. Concluding Remarks

Remote plasma sources (RPSs) are employed in semiconductor device manufacturing to provide a nearly charge-free source of, for example, halogen radicals for chamber cleaning and

isotropic etching. The toroidal transformer coupled plasma (TTCP) is an efficient RPS for delivering high power densities when using highly attaching gases. Results were discussed from a 2-dimensional computational investigation of single-ferrite core and dual-ferrite core TTCPs sustained in Ar, $NF_3$ and Ar/$NF_3$ mixtures. In single-ferrite core configurations, the secondary of the transformer represented by the plasma consists of a closed conduction current loop with plasma properties (electron density, power deposition) having azimuthal symmetry. Current in the secondary is carried dominantly by electron conduction. When using a dual-ferrite core configuration, geometrical limitations result in power deposition and plasma densities that have local maxima. Although there is a closed plasma current loop, the current is carried by a combination of conduction and displacement current.

Operation in Ar/$NF_3$ mixtures substantially altered the discharge topology, a consequence of depletion of the upstream electron density due to dissociative attachment to $NF_3$ and its dissociation fragments. When operating in $NF_3$, the maximum in electron density migrated downstream to where dissociation of the $NF_3$ and subsequent decrease in attachment enabled the plasma to be sustained. The upper volume of the plasma source contained a low density ($10^{10}$ - $10^{11}$ $cm^{-3}$) $F^-/NF_x^+$ ion-ion plasma. When increasing the $NF_3$ mole fraction in Ar/$NF_3$ mixtures, the plasma becomes more confined with a higher gas temperature. That higher gas temperature contributes to radical production through thermal dissociation of the $NF_3$.

Perhaps the greatest uncertainties in this investigation center on thermodynamics and heat transfer, particularly with electronegative gas mixtures in which power deposition can be highly confined. The local gas heating resulting from the confined power deposition produces local rarefaction of the gas which increases E/N, leading to more heating and more rarefaction. This is potentially an unstable condition that in other discharges produces arcs and constriction. In this device, heat transfer to the walls of the plasma stabilizes this potential instability. However, that stabilization is sensitive to heat conduction through the plasma, and the temperature of and heat transfer through the bounding materials. The heat transfer is sensitive to the thermal conductivities of the bounding materials and cooling of the device. The heat conduction through the plasma is sensitive to transport coefficients of the dissociation fragments which are poorly known. For the usual operating conditions, we do not expect the flow to be turbulent, however, the onset of turbulence would add additional uncertainties.

With the goal of having total dissociation of the feedstock halogen donor, there are several

tradeoffs that are made. For example, increasing flow rate produces a more confined plasma at a lower location in the device, which may then have less favorable transformer coupling. Total power deposition will normally scale with halogen flowrate so that the specific energy deposition (eV/molecule) remains above a critical value. An added benefit of this scaling is maintaining the spatial distribution of the plasma to have favorable transformer coupling.

**Acknowledgements**

This work was supported by MKS Instruments, the U.S. Department of Energy Office of Fusion Energy Sciences (DE-SC0020232), and the National Science Foundation. (CBET-2032604).

**Conflict of Interest**

The authors have no conflicts of interest to disclose.

**Data Availability**

The data that support the findings of this study are contained in the paper and available from the corresponding author upon reasonable request.

## References


[1] M. V. Donnelly and A. Kornblit. "Plasma etching: Yesterday, today, and tomorrow", *Journal of Vacuum Science Technology A* **31,** 050825, (2013). doi: 10.1116/1.4819316.

[2] S. Rauf, A. Balakrishna, Z. Chen, and K. Collins. "Model for a transformer-coupled toroidal plasma source", *Journal of Applied Physics* **111**, 023306, (2012). doi: 10.1063/1.3679565.

[3] T. F. Wu, L. C. Yu, A. Kumari, R. Z. Hung, and P. J. Chen. "Design and Implementation of Remote Plasma Sources for Semiconductor Chamber Cleaning", *ECCE 2020 - IEEE Energy Conversion Congress and Exposition*, pages 463–470, (2020). doi: 10.1109/ECCE44975.2020.9235422.

[4] S. P. Gangoli, A. D. Johnson, A. A. Fridman, R. V. Pearce, A. F. Gutsol, and A. Dolgopolsky. "Production and transport chemistry of atomic fluorine in remote plasma source and cylindrical reaction chamber", *Journal of Physics D: Applied Physics* **40**, 5140 (2007). doi: 10.1088/0022-3727/40/17/020.

[5] S. Raoux, T. Tanaka, M. Bhan, H. Ponnekanti, M. Seamons, T. Deacon, L.-Q. Xia, F. Pham, D. Silvetti, D. Cheung, K. Fairbairn, A. Jonhson, R. Pearce, and J. Langan. "Remote microwave plasma source for cleaning chemical vapor deposition chambers: Technology for reducing global warming gas emissions", *Journal of Vacuum Science Technology B: Microelectronics and Nanometer Structures* **17**, 477 (1999). doi: 10.1116/1.590580.

[6] B. Thedjoisworo, D. Cheung, and V. Crist. "Comparison of the effects of downstream $H_2$ - and $O_2$ -based plasmas on the removal of photoresist, silicon, and silicon nitride", *Journal of Vacuum Science Technology B* **31,** 021206, (2013). doi: 10.1116/1.4792254.

[7] B. A. Thedjoisworo, D. Cheung, and D. Zamani. "Characterization of hydrogen–plasma interactions with photoresist, silicon, and silicon nitride surfaces", *Journal of Vacuum Science Technology A* **30**, 031303 (2012). doi: 10.1116/1.4705512.

[8] S. Fujimura, K. Shinagawa, M. Nakamura, and H. Yano. "Additive Nitrogen Effects on Oxygen Plasma Downstream Ashing", *Japanese Journal of Applied Physics* **29**, 2165 (1990). doi: 10.1143/JJAP.29.2165.

[9] V. Volynets, Y. Barsukov, G. Kim, J-E. Jung, S. K. Nam, K. Han, S. Huang, and M. J. Kushner. "Highly selective $Si_3N_4/SiO_2$ etching using an $NF_3/N_2/O_2/H_2$ remote plasma. I. Plasma source and critical fluxes", *Journal of Vacuum Science Technology A* **38**, 023007 (2020). doi: 10.1116/1.5125568.

[10] V. Renaud, C. Petit-Etienne, J. P. Barnes, J. Bisserier, O. Joubert, and E. Pargon. "Two-step cycling process alternating implantation and remote plasma etching for topographically selective etching: Application to $Si_3N_4$ spacer etching", *Journal of Applied Physics* **126**, 243301 (2019). doi: 10.1063/1.5131030.

[11] S. Barnola, C. Vizioz, S. Borel, P. Gautier, C. Arvet, T. Chevolleau, T. Ernst, B. Guillaumot, N. Vulliet, C. Dupre, and E. Bernard. "Dry Etch Challenges in Gate All Around Devices for sub 32 nm Applications", *ECS Meeting Abstracts* **37**, 2478 (2008). doi: 10.1149/ma2008-02/37/2478.

[12] S. Borel, C. Arvet, J. Bilde, V. Caubet, and D. Louis. "Control of selectivity between SiGe and Si in isotropic etching processes", *Japanese Journal of Applied Physics* **43**, 3964 (2004). doi: 10.1143/JJAP.43.3964.

[13] B. E. E. Kastenmeier, B E E, Matsuo, P J, Beulens, and G. S. Oehrlein. "Chemical dry etching of silicon nitride and silicon dioxide using $CF_4/O_2/N_2$ gas mixtures", *Journal of Vacuum Science Technology A* **14**, 2802 (1996). doi: 10.1116/1.580203.

[14] B. E. E. Kastenmeier, P. J. Matsuo, G. S. Oehrlein, and J. G. Langan, "Remote plasma etching of silicon nitride and silicon dioxide using $NF_3/O_2$ gas mixtures", *Journal of Vacuum Science Technology A* **16**, 2047 (1998). doi: 10.1116/1.581309.

[15] H. C. M. Knoops, K. Arts, J. W. Buiter, L. M. Martini, R. Engeln, D. T. Hemakumara, M. Powell, W. M. M. Kessels, C. J. Hodson, and A. O'Mahony. "Innovative remote plasma source for atomic layer deposition for GaN devices", *Journal of Vacuum Science Technology A* **39**, 062403, (2021). doi: 10.1116/6.0001318.

[16] H. B. Profijt, P. Kudlacek, M. C. M. van de Sanden, and W. M. M. Kessels. "Ion and Photon Surface Interaction during Remote Plasma ALD of Metal Oxides", *Journal of The Electrochemical Society* **158**, G88, (2011). doi: 10.1149/1.3552663.

[17] C. M. Lin, H. C. Chang, Y. T. Chen, I. H. Wong, H. S. Lan, S. J. Luo, J. Y. Lin, Y. J. Tseng, C. W. Liu, C. Hu, and F. L. Yang. "Interfacial layer-free $ZrO_2$ on Ge with 0.39-nm EOT, $\kappa$=43, $2\times10^{-3}$ A/cm$^2$ gate leakage, SS =85 mV/dec, Ion/Ioff =6×105, and high strain response", *Technical Digest - International Electron Devices Meeting, IEDM*, pages 23.2.1–23.1.4, (2012). doi: 10.1109/IEDM.2012.6479086.

[18] K. S. A. Butcher, A. Fifuddin, P. P. T. Chen, and T. L. Tansley. "Studies of the plasma related oxygen contamination of gallium nitride grown by remote plasma enhanced chemical vapour deposition." *Physica Status Solidi C: Conferences* **160**, 156 (2002), doi: 10.1002/pssc.200390012.

[19] E. Pargon, C. Petit-Etienne, L. Youssef, G. Thomachot, and S. David. "New route for selective etching in remote plasma source: Application to the fabrication of horizontal stacked Si nanowires for gate all around devices", *Journal of Vacuum Science Technology A* **37**, 040601 (2019). doi: 10.1116/1.5100087.

[20] B. Bai and H. Sawin. "Neutral gas temperature measurements within transformer coupled toroidal argon plasmas", *Journal of Vacuum Science Technology A: Vacuum, Surfaces, and Films*, **22**, 2014–2021, (2004). doi: 10.1116/1.1778404.

[21] V. Godyak. "Ferromagnetic enhanced inductive plasma sources", *J. Phys. D: Appl. Phys*. **46,** 283001 (2013). doi: 10.1088/0022-3727/46/28/283001

[22] J.-F. Chien, C.-H. Chen, J.-J. Shyue, and M.-J. Chen. "Local Electronic Structures and Electrical Characteristics of Well-Controlled Nitrogen-Doped ZnO Thin Films Prepared by Remote Plasma In situ Atomic Layer Doping", *ACS Appl. Mater. Interfaces* **4**, 3471 (2012). doi: 10.1021/am300551y.

[23] S. Huang, V. Volynets, J. R. Hamilton, S. K. Nam, I.-C. Song, S. Lu, J. Tennyson, and M. J. Kushner. "Downstream etching of silicon nitride using continuous-wave and pulsed remote plasma sources sustained in $Ar/NF_3/O_2$ mixtures", *Journal of Vacuum Science Technology A* **36**, 021305 (2018). doi: 10.1116/1.5019673.

[24] H. Li, Y. Zhou and V. M. Donnelly, "Optical and mass spectroscopic measurements of dissociation in low frequency, high density, remote source $O_2$/Ar and $NF_3$/Ar plasmas", ", *Journal of Vacuum Science Technology A* **38**, 023011 (2020). doi: 10.1116/1.5126429.

[25] H. J. Yeom, D. H. Choi, Y. S. Lee, J. H. Kim, D. J. Seong, S. J. You and H. C. Lee, "Plasma density measurement and downstream etching of silicon and silicon oxide in an $Ar/NF_3$ mixture remote plasma source.", *Plasma Sci. Technol.* **21**, 064007 (2019), doi: 10.1088/2058-6272/ab0bd3

[26] K.-Y. Lin, C. Preischl, C. F. Hermanns, D. Rhinow, H.-M. Solowan, M. Budach, K. Edinger, and G. S. Oehrlein, "$SiO_2$ etching and surface evolution using combined exposure to $CF_4/O_2$ remote plasma and electron beam", *Journal of Vacuum Science Technology A* **40**, 063004

(2022). doi: https://doi.org/10.1116/6.0002038.

[27] S. Saloum, M. A. Zrir, B. Alkhaled, S. A. Shaker, Y. Balloul, D. Ghannoum, and M. N. Alkafri. "Study of silicon surface micro-roughness generated by $SF_6$ remote plasma etching." *Surface and Interface Analysis* **55,** 357 (2023). doi: 10.1002/sia.7198.

[28] I. Adamovich et al., "The 2022 Plasma Roadmap: low temperature plasma science and technology", *Journal of Physics D: Applied Physics* **55**, 373001 (2022). doi: 10.1088/1361-6463/ac5e1c.

[29] B. Bai, H. H. Sawin, B. A. Cruden, "Neutral gas temperature measurements of high-power-density fluorocarbon plasmas by fitting swan bands of $C_2$ molecules", *J. Appl. Phys.*, **99**, 013308 (2006), doi: 10.1063/1.2159545

[30] X. Chen, P. Loomis, E. Sevillano, and J. K. Yang, "High-Throughput Photoresist Strip Using a Toroidal RF Plasma Source in Ashers", *Semiconductor Magazine*, November:11, (2005). [https://www.mks.com/mam/celum/celum_assets/resources/toroidalTP.pdf?1]

[31] X. Chen, W. Holber, P. Loomis, E. Sevillano, S.-Q. Shao, S. Bailey, and M. Goulding. "Advances in Remote Plasma Sources For Cleaning 300 mm and Flat Panel CVD Systems", *Semiconductor Magazine*, August:6, (2003). [https://www.mks.com/mam/celum/celum_assets/resources/PRGcvdcleanTP.pdf?1]

[32] M. J. Kushner., "Hybrid modelling of low temperature plasmas for fundamental investigations and equipment design", *Journal of Physics D: Applied Physics* **42**, 194013 (2009). doi: 10.1088/0022-3727/42/19/194013.

[33] J. O. Hirschfelder, C. F. Curtis and R. B. Bird, "Molecular Theory of Gases and Liquids", (John Wiley and Sons, New York, 1964), Ch. 8.

[34] S. H. Song and M. J. Kushner. "Control of electron energy distributions and plasma characteristics of dual frequency, pulsed capacitively coupled plasmas sustained in Ar and $Ar/CF_4/O_2$." *Plasma Sources Science and Technology*, **21**, 055028, (2012). doi:10.1088/0963-0252/21/5/055028.

[35] N. A. Dyatko, Y. Z. Ionikh, I. V. Kochetov, D. L. Marinov, A. V. Meshchanov, A. P. Napartovich, F. B. Petrov, and S. A. Starostin. "Experimental and theoretical study of the transition between diffuse and contracted", *J. Phys. D: Appl. Phys* **41**, 55204 (2008). doi: 10.1088/0022-3727/41/5/055204.

[36] P. Tian and M. J. Kushner. "Controlling VUV photon fluxes in low-pressure inductively coupled plasmas", *Plasma Sources Science and Technology* **24**, 34017 (2015). doi: 10.1088/0963-0252/24/3/034017.

[37] J. R. Hamilton, J. Tennyson, S. Huang, and M. J. Kushner. "Calculated cross sections for electron collisions with $NF_3$, $NF_2$ and NF with applications to remote plasma sources", *Plasma Sources Science and Technology* **26**, 065010 (2017). doi: 10.1088/1361-6595/aa6bdf.

[38] S. Huang, V. Volynets, J. R. Hamilton, S. Lee, I.-C. Song, S. Lu, J. Tennyson, and M. J. Kushner. "Insights to scaling remote plasma sources sustained in $NF_3$ mixtures", *Journal of Vacuum Science Technology A* **35**, 031302 (2017). doi: 10.1116/1.4978551.

[39] V. Lisovskiy, V. Yegorenkov, P. Ogloblina, J. P. Booth, S. Martins, K. Landry, D. Douai, and V. Cassagne. "Electron transport parameters in $NF_3$", *Journal of Physics D: Applied Physics* **47**, 115203 (2014). doi: 10.1088/0022-3727/47/11/115203.

[40] M. Hayashi, "Recommended Values of Transport Cross Sections for Elastic and Total Collision Cross Section for Electrons in Atomic and Molecular Gases", Report No. IPPJ-AM-19. Technical report, Nagoya Institute of Technology, (1981). [http://dpc.nifs.ac.jp/IPPJ-

AM/IPPJ-AM-19.pdf]

[41] K. Tachibana. "Excitation of the $1s_5$, $1s_4$, $1s_3$ and $1s_2$ levels of argon by low-energy electrons", *Physical Review A*, **34**, 451 (1986). doi: 10.1103/PhysRevA.34.1007.

[42] D. Rapp and P. Englander-Golden. "Total Cross Sections for Ionization and Attachment in Gases by Electron Impact. I. Positive Ionization", *The Journal of Chemical Physics*, **43**, 1464 (1965). doi: 10.1063/1.1696957.

[43] A. Bogaerts, R. G. V. Serikov, and V. V. Serikov. "Calculation of gas heating in direct current argon glow discharges", *Journal of Applied Physics* **87**, 8334 (1999). doi: 10.1063/1.373545.

[44] L. A. Viehland and E. A. Mason, and. "Transport Properties of Gaseous Ions Over a Wide Energy Range, IV", *Atomic Data and Nuclear Data Tables* **60**, 37 (1995). doi: 10.1006/adnd.1995.1004 .